Technische Universität München

Lehrstuhl für Theoretische Biophysik

Auditory Information Processing. Detection, Invariant Coding & Connectivity

Hannes Lüling

Vollständiger Abdruck der von der Fakultät für Physik der Technischen Universität München zur Erlangung des akademischen Grades eines Doktors der Naturwissenschaften genemigten Dissertation.

Vorsitzender:
Univ.-Prof. Dr. Friedrich Simmel

Prüfer der Dissertation:
1. Univ.-Prof. Dr. J. Leo van Hemmen
2. Univ.-Prof. Dr. Christian Leibold (Ludwig-Maximilians-Universität München)

Die Dissertation wurde am 16.03.2012 bei der Technischen Universität München eingereicht und durch die Fakultät für Physik am 22.06.2012 angenommen.

To Carolin

Preface

Thesis organization

Chapters 2, 3 and 4 describe parts of the auditory pathway, while in Chapters 3, 4 and 5 information theory is used. As there is no direct link between Chapters 2 and 5, each of the chapters is introduced and discussed separately in place. A general prolog and epilog envelope this thesis.

Marginal notes are summaries of the main text to which they are aligned. Going through the marginal notes, after having read the main text, should serve an efficient way to refresh one's memory. Going through the marginal notes, the figures and their captions only (all in gray), the reader should be able to grasp the main ideas of this work.

Programming

All computer code, that was written for this thesis, is available on request to the author (mail@hanneslueling.de).

Funding

Funding was provided by the Bundesministerium für Forschung und Bildung (grant number: 01GQ0440).

Contributions

Chapter 2. J. Leo van Hemmen contributed in a general sense. Jan-Moritz P. Franosch contributed to programming and analyses. The content was published with the collaborators as *A two-dimensional cochlear fluid model based on conformal mapping* [1].

Chapter 3. Benedikt Grothe contributed in a general sense. Ida Siveke [2] did the recordings. Christian Leibold contributed the principal part of the conception, part of the analysis and writing of the article, which was published with the collaborators as *Frequency-Invariant Representation of Interaural Time Differences in Mammals* [3].

Chapter 4. Katrin Vonderschen did the recordings [4]. Christian Leibold contributed to the conception.

Chapter 5. Álvaro Tejero Cantero, Anna Schützenberger and Chun-Wei Yuan contributed to the conception and programming. Christian Leibold contributed to the conception.

Acknowledgements

I'd like to thank all collaborators for their scientific contributions, most of all my supervisor Christian Leibold!

Yet not to be underestimated is the *emotional* contribution from my colleagues Michael Bendels, Moritz Franosch, Simon Lehnert, Christian Leibold, Lu Li, Alexander Loebel, Axel Kammerer, Alexander Mathis, Gonzalo Otazu, Philipp Rautenberg, Álvaro Tejero, Kay Thurley, Andreas Vollmayr, Chun-Wei Yuan (in alphabetical order). They made my workdays!

Of course I'd like to also thank my family and friends outside university for their invaluable support!

Contents

Chapter 1

Prolog

Imagine sitting in a concert hall, awaiting Mozart's fifth and last violin concerto to be performed. The conductor takes a short pause, before slowly lifting his baton to indicate the entry.

The first movement opens with the orchestra playing the main theme. As you close your eyes, the solo violin comes in with a short adagio passage in A major carried by a simple accompaniment of the orchestra. The subtle vibrations of the soundboard synchronize with the air around it. These sound waves, composed of various frequencies, permeate and reverberate through the entire concert hall, and undulate toward a listener's ears at a speed of about 340 meters per second to enter them in enormously quick succession. At the end of the auditory canal, the sound waves reach the ear drum, which marks the beginning of the middle ear.

Vibrations of the ear drum are passed to three delicate bones – hammer, anvil and stirrup. Adjusted by muscles, these bones transfer sound energy from the air to the fluids of the cochlea, the auditory portion of the inner ear.

Fluid pressure differences lead to deflections of the basilar membrane, a structure running along the coil of the cochlea. The physiology of the basilar membrane changes from its basal to its apical end, which has a crucial influence on the size of deflection. Each frequency the music is composed of, is hereby mapped onto a different place along the basilar membrane. Deflections lead to a shear on

Chapter 2 is about *Sound decomposition in the cochlea.*

the inner and outer hair cells, which are distributed along the basilar membrane. This shear opens transduction channels, allowing ions of the cochlear fluid to enter the hair cells. The ion influx into outer hair cells causes conformational changes of motor proteins driving oscillations in the length of cells. These oscillations occur at the frequency of the sound, providing mechanical feedback amplification. The ion influx into inner hair cells triggers the release of neurotransmitters, which diffuse across a narrow space to bind to receptors of the innervating cochlear nerves. This causes a rise in the membrane potential that eventually increases to a threshold value followed by the opening of ion channels. The process proceeds rapidly, resulting in an action potential that propagates along the cochlear nerve.

Action potentials are the means by which a person's 100 billion nerve cells exchange information via more than 100 trillion connections.

Through intermediate stations information reaches the superior olivary complex, where inputs coming from both ears are integrated. Within the superior olivary complex lies the medial superior olive. Neurons of the medial superior olive compare precisely timed action potentials arriving from both ears. The time differences contain information about the arrival times of the sound at the listener's ears. As the listener is seated on the left of the concert hall, but is looking straight ahead, the sound reaches his right ear some milliseconds earlier. Astonishingly, this minute time difference is about two orders of magnitude below that of the duration of the action potential encoding it.

Chapter 3 is about *Mammalian frequency-invariant sound localization.*

Information about the location of the violinist is then forwarded through further stations to the dorsal nucleus of the lateral lemniscus, which passes it on to the inferior colliculus. The inferior colliculus additionally receives information from the superior olivary complex, integrates it, and transfers it through the thalamus

to the primary auditory cortex.

This way of auditory information processing is unique to mammals, however, different species have independently evolved similar solutions driven by the same evolutionary constraints. More than 200 million years ago, the ancestors of today's birds evolved an auditory system allowing them to hear and to localize sound.

The pallium, which is outermost to mammalian and avian brains, contains characteristic distributions of neuron types and connections with other pallial and subpallial regions. It is the intricate and still insufficiently known interconnection of nerve cells that permits information integration allowing one to perceive separate attributes of Mozart's music in its prodigious entirety.

Chapter 4
compares mammalian to *Avian frequency-invariant sound localization.*

Chapter 5
describes *A method to estimate network connectivity.*

Chapter 2

Sound decomposition in the cochlea

2.1 Introduction

The cochlea is a spiral-shaped bony cavity of the inner ear that is hollowed out of the temporal bone of the scull (figure 2.1, upper panel). The essential element of the cochlea is the organ of Corti, the sensory organ of hearing, which is distributed along the partition separating the fluid filled chambers in the coiled tube of the cochlea (figure 2.2, upper panel). The watery liquid enclosed by the cochlea moves in response to the vibrations coming from the middle ear (figure 2.1, lower panel) via the oval window. Fluid-pressure differences lead to oscillation of the cochlear partition. Since the physiology of the cochlear partition systematically changes from its basal to its apical end, sound is decomposed along the cochlear partition. The resulting shears on hair cells inclosed by the organ of Corti opens transduction channels, allowing the ions of the cochlear fluid to enter the cells (figure 2.2, lower panel). The inner hair cells release neurotransmitters that bind to receptors of innervating nerve fibers that emit action potentials. The ion influx into the outer hair cells triggers active vibrations of cell bodies providing mechanical feedback amplification.

In a nutshell, the cochlea decomposes sound and transfers it into

The *Cochlea* is the spiral-shaped fluid-filled cavity of the inner ear. It transforms sound according to its frequencies into electrical signals.

Pressure oscillations are transferred to the cochlear fluids via the *oval window*. The *round window* allows the fluids to move.

The *cochlear partition* is the tissue stretched in the fluids along the cochlea and place of the organ of hearing.

Variations of the mechanical properties of the cochlear partition enable decomposition of sound.

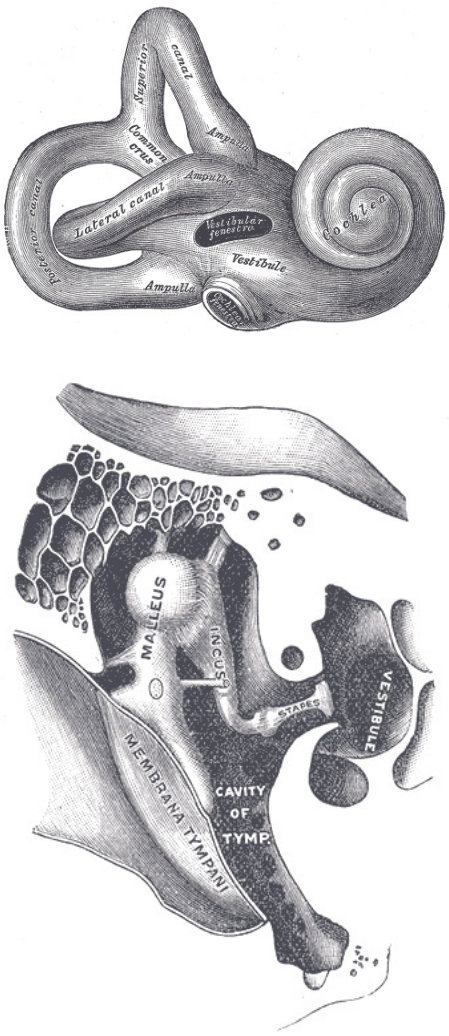

Figure 2.1: Upper panel: Inner Ear. The inner ear is hollowed out of temporal bone of the scull. The spiral-shaped part is a drawing of the cochlea. Sounds are transmitted to the cochlear fluids by the footplate of the stapes (lower panel) that is attached to the membrane covering the oval window (vestibular fenestra). The round window (cochlear fenestra) is also covered by a membrane allowing the fluids to move. Lower panel: Middle ear with ossicles. The ossicles hammer (malleus), anvil (incus) and stirrup (stapes) serve to transmit sounds from the air to the fluid filled cochlea. The malleus is attached to the eardrum (membrana tympani), a membrane that closes off the middle ear. The stapes' footplate is attached to a membrane covering the oval window (membrana vestibularis). (Image adapted from [5])

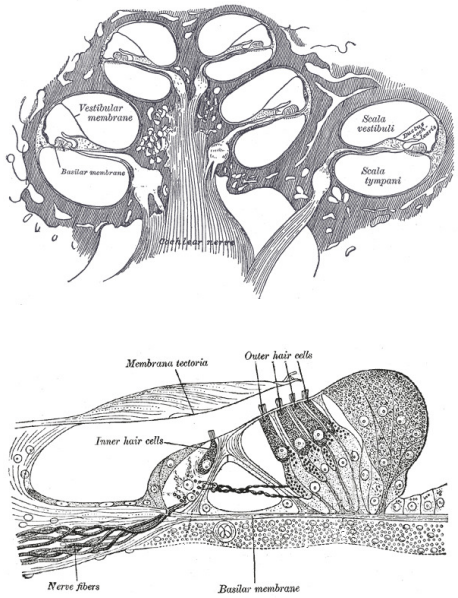

Figure 2.2: Upper panel: Cross section of the Cochlea. The cochlear fluids of scala vestibuli and ductus cochlearis are separated by the vestibular membrane (membrana vestibularis). The scala tympani is separated from the ductus cochlearis by the basilar membrane except for the helicotrema, which is a tiny hole at the apical end of the cochlea. Pressure differences across the basilar membrane make it move and with it the attached organ of Corti (see lower panel). Lower panel: Cochlear partition. On top of the basilar membrane, the organ of Corti is located that incloses the inner and the outer hair cells. Inner hair cells transform motion of the cochlear partition into electrical signals that are then relayed via the nerve fibers upstream for further processing. Outer hair cells, that touch the membrana tectoria, provide amplification. (Images adapted from [5])

electrical signals that are forwarded to the auditory brainstem and to the auditory cortex for further processing.

An appropriate mathematical model for the cochlear partition not only has to capture its mechanical properties, but also its intricate interaction with the fluids in which it is immersed. This interaction crucially complicates the task.

There were plenty of models put forward [6, 7, 8, 9, 10, 11, 12, 13, 14], many of which utilize the long-wave approximation [11] and short-wave approximation [10, 12]. These theories assume the local wave length of the cochlear partition to be long or short, respectively, as compared to the duct's (scala vesibuli and ductus cochlearis together) height. Both assumptions fail either near the resonance region, i.e. the place of maximal displacement of the cochlear partition, or far away from it [13]. All these approximative theories have been reviewed by Wever [15] and, more recently, by Sireoka, who additionally discusses a composition of the long-and short-wave approximation [13].

Beyond the above mentioned approximations, there are attempts to model the cochlea analytically for different dimensions.

Grossly unrealistic one-dimensional models can nevertheless give a good prediction of cochlear response [8], but because of substantial simplifications prevent studying fluid effects.

In order to account for fluid motion more accurately, two-dimensional theories have been put forward, with Siebert [12] and Allen [6] leading the way. Deriving integral equations, both approaches reduce the problem by one dimension. Siebert, after all, has solved it by applying the short-wave approximation. Allen has to approximate the limit of an infinite sum.

Three-dimensional models [16] appear to be analytically unfeasible, as long as dimensionality is not reduced. Much of the three-dimensional work [17, 14, 18, 19, 20, 21] requires simplifications, which deny much of the physiological reality of the cochlea [22].

Here a novel two-dimensional cochlear fluid model is presented, based on conformal mapping. Although the conformal-mapping method is well-known in fluid dynamics, its application to cochlear modeling is novel. This method is both analytically and numerically simple in comparison to alternative methods, e.g. finite differences and image methods, and does not require approximations that are intrinsic to some methods, e.g. long-wave and short-wave models. Under the assumptions of an inviscid, irrotational and incompressible fluid, the problem is reduced to solving the Laplace equation with boundary conditions prescribed by the geometry, as explained in detail in the next paragraph. Applying the technique of conformal mapping simplifies this boundary value problem substantially, since it allows for the reduction of a complicated boundary value problem to an easy one, solely by transforming a known solution through the proper conformal mapping. The result is an equation of motion that is exact and entirely analytic within the geometric and hydrodynamic approximations described above. It is solved numerically in order to obtain the time-dependent motion of the cochlear partition, given the acceleration of the stapes. The advantage of an analytically derived equation of motion is that it can be easily modified, so that one can investigate the significance of different physical effects on cochlear motion. For instance, the results below confirm, that hydrodynamic coupling plays an important role in sharpening the response of the cochlear partition to pure tones. In particular, strengthening hydrodynamic coupling makes the resonant frequency response increasingly asymmetric.

2.2 A novel box model

2.2.1 Simplified geometry

The cochlea is simplified to a flat box with an open side (round window) and three closed sides (bony wall, oval window and cochlear partition).

The difficult three-dimensional problem is simplified by assuming that the cochlea is an one-sided open two-dimensional box as in Figure 2.3. This is achieved by "unfolding" the cochlea in the following way: First the snail-shaped duct is unrolled so that it becomes straight and has the shape indicated by the dashed lines in Figure 2.3. The cochlear partition still divides the duct in the middle such that the two fluid-filled parts are connected by the *helicotrema*. It is assumed that the exact form of the fluid flow through the helicotrema is negligible so that, in good approximation, one can further unfold the duct along the semi-infinite lines. The result is a rectangular box with one open side representing the round window. The closed side on the opposite end represents the oval window connected to the stapes footplate. The closed side on the left in figure 2.3 is the unfolded bony wall. The closed side on the right consists of twice the cochlear partition. Finally the inward dimension is neglected.

As the resulting geometry now represents the cochlea partition *twice*, any motion of the cochlear partition must be symmetric about the point $(H/2, L)$, which is the former apical end of the cochlear partition. Except for one side being open, the resulting model geometry is equivalent to J. B. Allen's [6]. One open side approximates the physics of the cochlea better than fully enclosed cavities since the round window is in fact flexible. If it were not, incompressibility would not allow fluid motion at all.

2.2.2 Physics

Elastic coupling between adjacent parts of the cochlear partition is negligible [9]. Assuming sufficiently small displacements, one

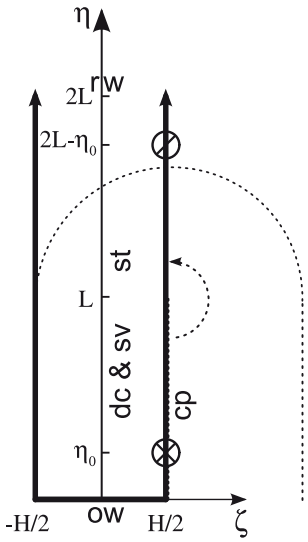

Figure 2.3: Flat Box model of the cochlea. rw (round window), ow (oval window), cp (cochlear partition), dc & sv (ductus cochlearis) and (scala vestibuli) unified, st (scala tympani). The figure shows an abstract cochlea structure both in its unfolded (solid line) and original (dashed line) shape. The basilar membrane is at position $\zeta = H/2$, the oval window at position $\eta = 0$, the round window at position $\eta = 2L$. The effect of the vestibular membrane (membrana vestibularis) is acoustically negligible [16]. Therefore, the two ducts dc and sv are assumed identical. The original cochlea structure (dashed lines) is "unfolded" along the dashed half-circle shaped arrow, so as to get a straight one (solid lines) with effectively open boundary conditions at $\eta = 2L$, instead of the dashed U-turn at originally $\eta = L$. This leads to a double representation of the basilar membrane, namely one from 0 to L and one from L to $2L$. Any motion of the cochlear partition at η_0 (circled plus) thus coincides with an opposite motion at $2\,L - \eta_0$ (circled minus). Motions lead to flux sources and sinks. The round window is represented by an effluent at $2L$.

The cochlear partition is simplified to a continuum of damped linear oscillators, that are driven by fluid pressure differences.

can therefore describe the motion of the cochlear partition by a continuum of damped linear oscillators,

$$m\left(\eta\right)\frac{\partial^2\gamma}{\partial t^2}\left(\eta,t\right)+h(\eta)\frac{\partial\gamma}{\partial t}\left(\eta,t\right)+k\left(\eta\right)\gamma\left(\eta,t\right)=f\left(\eta,t\right) \tag{2.1}$$

where $\gamma\left(\eta,t\right)$ is the partition's displacement at position η and time t. Mass m, damping h, stiffness k as well as the external force f are the corresponding quantities per unit of length. Amplification by outer hair cells are neglected here, albeit they could be introduced as undamping [23] by an additional term $-u(\eta)\,\partial\gamma(\eta,t)/\partial t$ in equation (2.19). The external force density arises from pressure differences across the cochlear partition and is thus written

$$f\left(\eta,t\right)=b\,\Delta p\left(\eta,t\right)=b\left[p(\eta,t)-p(2L-\eta,t)\right] \tag{2.2}$$

where b is the width of the cochlear partition and Δp is the difference between pressure right above and below it. The pressure difference is expressed by $\Delta p\left(\eta,t\right)=\left[p(\eta,t)-p(2L-\eta,t)\right]$ (figure 2.3). For simplicity the width and height of the duct are assumed to be constant here. As can be seen later, this assumption allows for creating analytic expressions for fluid forces and for a better understanding of the underlying physics without a fundamental change of the cochlea function .

In good approximation, the cochlear fluid is inviscid and incompressible [16]. Accordingly, the Euler equation of fluid motion [24] holds. As fluid motion is approximately irrotational [16], Bernoulli's equation

$$p=\rho\left(\frac{\partial\Phi}{\partial t}-\frac{1}{2}\,\boldsymbol{v}^2-V\right)+\text{const.} \tag{2.3}$$

applies, where $\boldsymbol{v}$ denotes fluid velocity, p pressure, ρ fluid density, V the gravity potential, and Φ the velocity potential determined by

$$\boldsymbol{v}=-\nabla\Phi\,. \tag{2.4}$$

The second term $\boldsymbol{v}^2$ in equation (2.3) is negligible [25, 26] compared to the first term. Taking the divergence on both sides of equation (2.4) and using the incompressibility condition $\operatorname{div} \boldsymbol{v} = 0$, one obtains the Laplace equation

$$\frac{\partial^2 \Phi}{\partial \zeta^2} + \frac{\partial^2 \Phi}{\partial \eta^2} = 0\,. \tag{2.5}$$

The problem of deriving the fluid pressure is reduced to solving the boundary value problem as determined by the flat box model of the cochlea.

The proper boundary conditions for the box specified in figure 2.3 are given by

$$-\left.\frac{\partial \Phi}{\partial \eta}\right|_{\eta=0} = v^S\,, \tag{2.6a}$$

$$\left.\frac{\partial \Phi}{\partial \zeta}\right|_{\zeta=-\frac{H}{2}} = 0\,, \tag{2.6b}$$

$$-\left.\frac{\partial \Phi}{\partial \zeta}\right|_{\zeta=\frac{H}{2}} = v^C \tag{2.6c}$$

where v^S is the stapes velocity and v^C the cochlear partition's velocity. Using Bernoulli's equation (2.3), one rewrites the force density (see equation (2.2)) in the form

$$f\,(\eta, t) = \rho b\, \frac{\partial \Delta\Phi}{\partial t}\,(\eta, t)\ . \tag{2.7}$$

Since the cochlear partition has zero thickness, the gravity potential V below and above the cochlear partition is identical, therefore $\Delta V = 0$. In the model of the unfolded duct, one then has to put

$$\Delta\Phi\,(\eta, t) = \Phi\,(\eta, t) - \Phi\,(2\,L - \eta, t) \tag{2.8}$$

as any motion of the cochlear partition at η coincides with an *opposite* motion at $2\,L - \eta$.

In order to gain an analytic solution of the Laplace equation (2.5) given the boundary conditions (2.6a–2.6b), ones takes advantage of

the method of conformal mapping. In the following, analytic maps from the complex w-plane where $w = \zeta + i\eta$, into the complex z-plane where $z = x + iy$ are used. Analytic functions are harmonic, so that they satisfy the Laplace equation (2.5), which one can verify with the help of the Cauchy-Riemann equations; cf. Churchill [27, chap. 2] and Titchmarsh [28, §§ 2.13–2.15 and 6.15 chap. VI]. Hence the analytic function

$$u(z) = \phi(z) + i\psi(z) \ , \tag{2.9}$$

the so-called complex potential, is a solution of the Laplace equation, too. Once one has an analytic function satisfying simple boundary conditions, the theory of conformal mapping allows for transforming the solution to different, and, supposedly, more complicated boundary conditions. The two following theorems prove essential for doing so.

The solution to a properly chosen boundary value problem is found and transformed by conformal mapping, such that it solves the boundary value problem of the flat box model of the cochlea.

Theorem 1. *Suppose that the analytic function*

$$g(w) = x(\zeta, \eta) + iy(\zeta, \eta)$$

maps a domain D_w in the w-plane onto a simply connected domain D_z in the z-plane. If $u(x, y)$ is a harmonic function defined on D_z, then the function

$$U(\zeta, \eta) = u[x(\zeta, \eta), y(\zeta, \eta)]$$

is harmonic in D_w [27].

The real part of the transformed complex potential is the velocity potential and the imaginary part is called the stream function (figure 2.5). The proof of the theorem makes use of the fact, that a composite function of two analytic functions is again analytic and thus harmonic [27].

Theorem 2. *Suppose that the analytic function*

$$g(w) = x(\zeta, \eta) + iy(\zeta, \eta)$$

maps some arc Γ *in the* w*-plane onto an arc* C *in the* z*-plane. Let* $g(w)$ *be conformal, i.e. analytic and* $g(w) \neq 0$ *on* Γ*, and let* $u(x, y)$ *be differentiable on* C*. If the function* $u(x, y)$ *satisfies either of the conditions*

$$u = \text{const.} \qquad \textit{or} \qquad \frac{\mathrm{d}u}{\mathrm{d}n} = 0$$

along C*, where the derivative is the normal derivative to* C*, then the function*

$$U(\zeta, \eta) = u[x(\zeta, \eta), y(\zeta, \eta)]$$

satisfies the corresponding condition along Γ*.*

The proof uses the fact, that conformal maps locally preserve angles [27, 28].

Suppose that the conformal function

$$g(w) = x(\zeta, \eta) + iy(\zeta, \eta)$$

maps an arc Γ in the w-plane onto an arc C in the z-plane, then the function

$$U(\zeta, \eta) = u[x(\zeta, \eta), y(\zeta, \eta)]$$

satisfies the corresponding condition along Γ [27, 28].

An infinitely long (vertical direction in figure 2.4) box of height H (horizontal direction in figure 2.4), with the side at infinity being open and with the opposite side overlapping with the real axis, is mapped onto the upper complex half plane [27] by the conformal map

$$g(w) = H \sin\left(\frac{\pi}{H}\, w\right) . \tag{2.10}$$

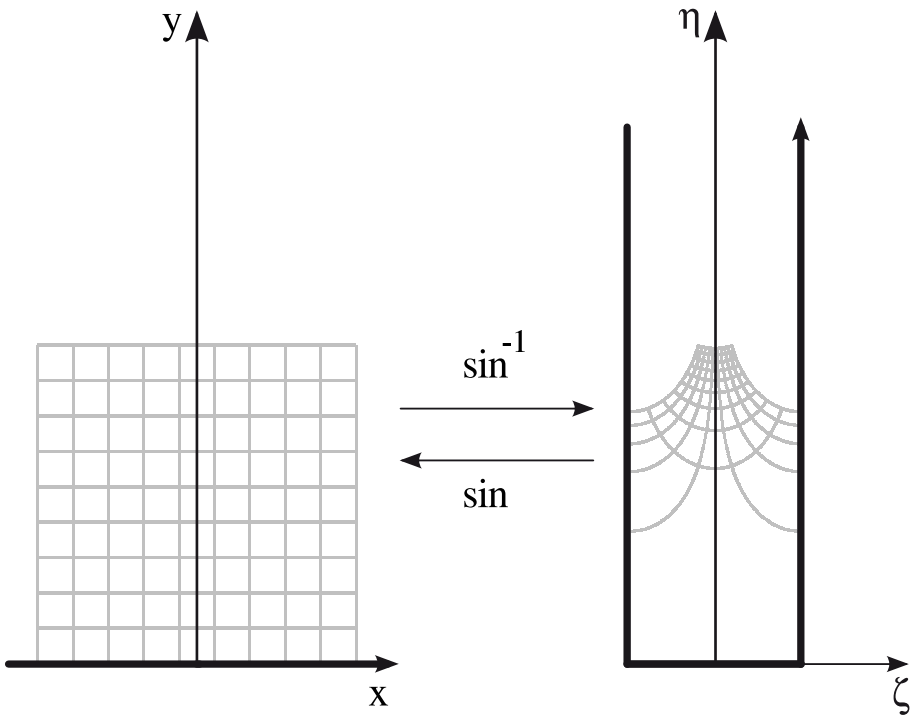

Figure 2.4: Generic illustration of conformal mapping. The sine function maps an infinitely long one-sided open box onto the upper complex half plane [27]. The inverse function maps the upper complex half plane onto the specified box. A globally perpendicular lattice in the upper half of the z-plane (left panel, gray) is thereby mapped onto a new lattice (right panel, gray) within the box in the w-plane. The perpendicularity of the lattice is only locally preserved. The x-axis (left panel, thick) is mapped onto the boundary of the specified box (right panel, thick).

The complex potential of a point source at z_0 with source strength q in an *unbounded* region is

$$u(z) = -\frac{1}{2\pi} q \ln(z - z_0) - \frac{1}{2\pi} q \left[\ln|z - z_0| + i \arg(z - z_0)\right] . \tag{2.11}$$

The complex potential of a distribution of point sources with density $q(z_0)$ along the arc C is therefore

$$u(z) = -\frac{1}{2\pi} \int_C q(z_0) \ln(z - z_0) \, \mathrm{d}z_0 . \tag{2.12}$$

Thus, according to the theorems above with $z = g(w)$, the complex potential of a distribution of point sources in the one-sided open box is

$$\begin{aligned} U(w) &= -\int_\Gamma Q(w_0) \ln\left[\sin\left(\frac{\pi}{H} w\right) - \sin\left(\frac{\pi}{H} w_0\right)\right] \\ &\times \cos\left(\frac{\pi}{H} w_0\right) \mathrm{d}w_0 \end{aligned} \tag{2.13}$$

where $Q(w_0)$ is the source distribution along the arc Γ. In equation (2.13), there are sources on the stapes as well as on the cochlear partition. The velocity potentials of the stapes and the cochlear partition is denoted by Φ^S and Φ^C, which are the real parts of the corresponding complex potential $U(w)$. Figure 2.5 shows a contour-plot for point sources. The oval window is part of the real axis and the cochlear partition is represented by the straight line given by $\zeta = H/2$ and $\eta \geq 0$. Using the identities $\sin w = \sin\zeta \cosh\eta + i \cos\zeta \sinh\eta$ and $\cos w = \cos\zeta \cosh\eta - i \sin\zeta \sinh\eta$, one obtains

$$\Phi^C(\eta, t) = \int_0^L Q^C(\eta_0, t) \, K^C(\eta, \eta_0) \sinh\left(\frac{\pi}{H}\eta_0\right) \mathrm{d}\eta_0. \tag{2.14}$$

The source strength densities $Q^C(\eta_0, t)$ on the cochlear partition result from its motion and thus

$$Q^C(\eta_0, t) = \frac{1}{\pi \sinh\left(\frac{\pi}{H}\eta_0\right)} \frac{\partial \gamma}{\partial t}(\eta_0, t) \tag{2.15}$$

where the factor $1/\sinh(\pi\eta_0/H)$ undoes the redistribution of the source strength density along the cochlear partition, caused by the transformation $z = g(w)$; (see equation (2.10)). The integration kernel K^C in equation (2.14),

$$\begin{aligned} K^C(\eta, \eta_0) = -\frac{1}{2\pi} \Big[& \ln \left| \cosh\left(\frac{\pi}{H}\eta\right) - \cosh\left(\frac{\pi}{H}\eta_0\right) \right| \\ & - \ln \left| \cosh\left(\frac{\pi}{H}\eta\right) - \cosh\left(\frac{\pi}{H}(2L - \eta_0)\right) \right| \Big] , \end{aligned} \tag{2.16}$$

assures that each motion at position η coincides with an opposite one at position $2L - \eta$.

Since a membrane spans the oval window, one may well assume that the stapes, moving with velocity $v^S(t)$, causes a cosine-like source density $v^S(t)\cos(\pi\zeta_0/H)$. In any case, a homogeneous flow is present shortly after the basal end. Through an appropriate substitution in equation (2.13) and, again, by considering the non-linear transformation of sources, one obtains

$$\begin{aligned} \Phi^S(\eta, t) &= -\int_{-H/2}^{H/2} v^S(t) \ln \left[\cosh\left(\frac{\pi}{H}\eta\right) - \sin\left(\frac{\pi}{H}\zeta_0\right) \right] \\ &\times \cos\left(\frac{\pi}{H}\zeta_0\right) \mathrm{d}\zeta_0 . \end{aligned} \tag{2.17}$$

Integrating equation (2.17) one finds

$$\Phi^S(\eta, t) = -\frac{H}{\pi} v^S(t) \left[(\chi + 1)\ln(\chi + 1) - (\chi - 1)\ln(\chi - 1) - 2 \right] \tag{2.18}$$

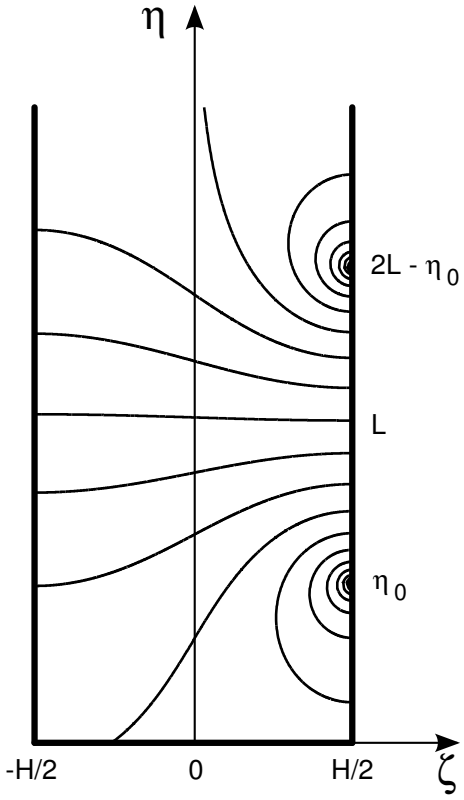

Figure 2.5: ISO-POTENTIAL LINES. Iso-potential lines as generated by a point source at η_0 and a point sink of the same absolute strength at $2\,L - \eta_0$. Fluid streams perpendicular to the iso-potential lines. Boundary conditions are fulfilled, as every contour hits the box's boundary perpendicularly (except at the bottom that was shifted upwards). Note, that the gradient, and, hence, the velocity is orthogonal to the contour. The height is adapted here for a better overview.

where $\chi(\eta) := \cosh(\pi/H\,\eta)$. For the sake of simplicity one writes $\Phi^S(\eta,t) =: Q^S(t)\,Y^S(\eta)$. As can be seen from figure 2.6, the stapes-fluid interaction $\Delta Y^S(\eta) := Y^S(\eta) - Y^S(2\,L-\eta)$ approaches a straight line shortly after the basal end.

The derived motion equation of fluid-pressure driven oscillators is reduced in dimension and entirely analytic.

Inserting the termes (2.14) and (2.18) into equations (2.7) and (2.1), one obtains an entirely analytic equation of motion for the cochlear partition,

$$\begin{aligned} m(\eta)\,\frac{\partial^2\gamma}{\partial t^2}(\eta,t) \;&+\; h(\eta)\,\frac{\partial\gamma}{\partial t}(\eta,t) + k(\eta)\gamma(\eta,t) = \\ \rho\,b\,\Delta Y^S(\eta)\,\frac{\mathrm{d}Q^S}{\mathrm{d}t}(t) \;&+\; \rho\,b\int_0^L \frac{\partial^2\gamma}{\partial t^2}(\eta_0,t)\,\Delta K^C(\eta,\eta_0)\,\mathrm{d}\eta_0 \end{aligned} \tag{2.19}$$

where $\Delta K^C(\eta,\eta_0) := K^C(\eta,\eta_0) - K^C(2\,L-\eta,\eta_0)$. Although the original hydrodynamic problem is two-dimensional, one is given a spatially one-dimensional equation of motion and there is no need not solve it for the fluid motion explicitly.

2.3 Results

2.3.1 Compulsory model features

Figure 2.6 shows $\Delta\bar{K}^C_{jk}$. The cochlea maps different frequencies to different positions along the basilar membrane, as in the simulations shown in figure 2.7.

The phases are mostly monotone functions of the cochlear position, as shown by figure 2.8, evoking the illusion of a wave traveling from stapes to helicotrema. Figure 2.8 also depicts the frequency dependence of the phase difference. The higher the frequency of the stimulus tone, the higher the maximum phase difference of resonating elements of the cochlear partition.

The model reproduces compulsory cochlear features, e.g. its frequency selectivity.

The presented model reproduces essential cochlear features, viz.

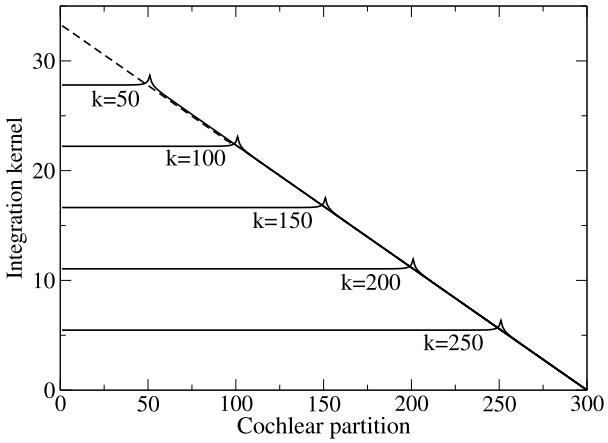

Figure 2.6: INTEGRATIONAL KERNEL. Each cochlear partition interacts with other cochlear partitions due to hydrodynamic coupling. Strength of hydrodynamic coupling of partition number k acting on partition number j is described by the integration kernel $\Delta\bar{K}^C_{jk}$ in equation (2.23). The solid graphs display $\Delta\bar{K}^C_{jk}$ for different k (50, 100, 150, 200, 250) depending on the cochlear partition number j, the position. The interaction has a maximum at $j = k$. That is, a cochlear partition interacts maximally with itself, which is physically equivalent to additional mass of the cochlear partition.

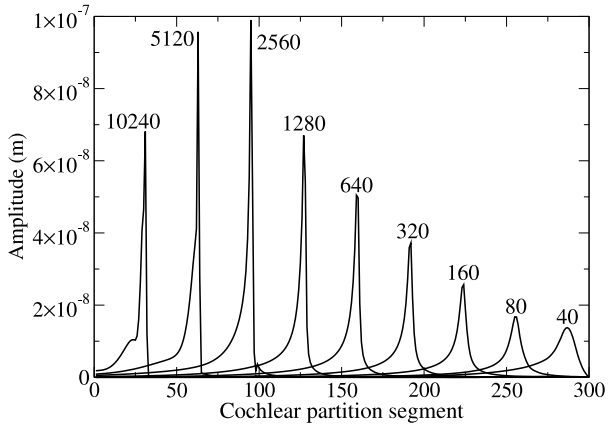

Figure 2.7: Envelopes of cochlear partition displacements. Amplitude depending on the position of the cochlear partition (element numbers 1–300) corresponding to the given frequencies (Hz) indicated at the maxima. The cochlea was excited by pure tones, starting with 20 Hz and doubling up to 10240 Hz, which shows the approximately logarithmic dependence of maximal amplitude upon the distance from the helicotrema at partition number 300.

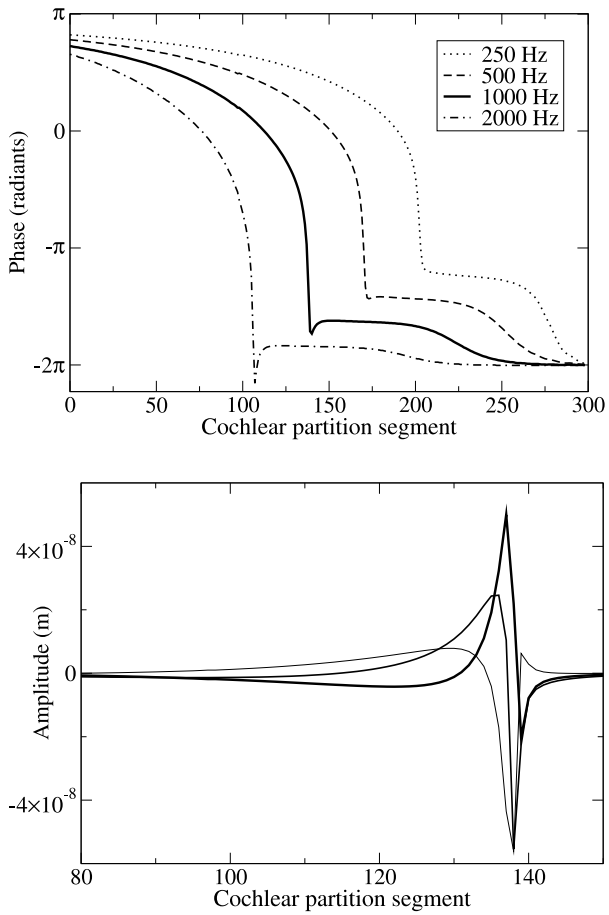

Figure 2.8: Upper panel: Phase of cochlear partition displacement. Phase depending on the element number of the cochlear partition for pure tone stimulations of 250, 500, 1000 and 2000 Hz. The mostly monotonically decreasing phases produce partition displacements, such that waves seem to travel from base to apex. Lower panel: Displacement of cochlear partition. Displacement depending on the element number of the cochlear partition for pure-tone stimulation with 1000 Hz for three successive moments of time (thin to thick line) with a time interval of 0.2 ms. For the observer a wave seems to travel in the direction from stapes (left) to helicotrema (right).

frequency selectivity, asymmetry of the envelope and a mostly monotonic phase. Deviations from previous results, i.e. places of resonance or phase differences of the traveling wave (two cycles [9] for 3.2 kHz input frequency, three cycles [6] for 1 kHz) are possibly due to the choice of functions of mass, damping and stiffness, which vary among species anyway, even between individuals. For a review of specific phase differences, see [29]. Moreover, different boundary conditions, in particular modeling of the round window as an open end of the duct, may also account for deviating results and need to be studied more accurately in the future.

The parameters used for all graphs are listed in Table 2.1. Figure 2.6 shows $\Delta\bar{K}^C_{jk}$. The cochlea maps different frequencies to different positions along the basilar membrane, as in the simulations shown in figure 2.7.

2.3.2 Comparison to the method of images

J. B. Allen [6] considered the same geometry used here, except that his boundary conditions do not allow for one of the sides being open, thus neglecting the presence of the round window. Taking advantage of the method of images, he found the Green's function, i.e., the real part of the complex potential generated by the cochlear partition, being given by the infinite sum

$$G^C(x, x_0) = -\frac{(-1)^j}{\pi} \sum_{j=0}^{\infty} \sum_{k=0}^{\infty} \ln\left[r^+_{j,k}(x, x_0)\, r^-_{j,k}(x, x_0) \right] \qquad (2.20)$$

with

$$r^{\pm}_{j,k}(x, x_0) = \sqrt{(x \pm x_0 + 2\,j\,L)^2 + (2\,k\,H)^2} \qquad (2.21)$$

instead of equation (2.16). The double sum stems from an infinite number of images of point sources and sinks. Since the exact limit of

The model overcomes inconsistent boundary conditions from a similar model based on the method of images.

the sum in equation (2.20) is unknown, the sum has to be truncated after a few terms. Moreover, when considering stapes motion, the method of images leads to an open duct, which is inconsistent. On the other hand, the method of conformal mapping allows for consistent and physically plausible boundary conditions.

2.3.3 Varying hydrodynamic coupling

Besides obvious reasons like shock absorbance and ion supply to hair cells, the cochlear fluid is supposed to improve frequency selectivity. By simple alteration of equation (2.25), one is able to quantitatively study the role of the cochlear fluid in regard to frequency selectivity (see Appendix). Thus, in order to understand the effect of coupling of the cochlea partition to itself through the cochlear fluid, $\bar{K}^C_{jk}$ for $j \neq k$ is replaced by $c \cdot \bar{K}^C_{jk}$ in equation (2.25), retaining the diagonal elements and reducing the influence of hydrodynamic coupling by off-diagonal elements for a coupling parameter $0 \leq c < 1$. Figure 2.9 shows the effect of hydrodynamic coupling of different cochlear partition segments by gradually reducing the coupling parameter c. Hydrodynamic coupling sharpens the frequency response, especially at the low frequency side. This is reasonable, since fluid pressure spreads instantaneously from the site a force is applied, pushing adjacent elements of the cochlear partition in the direction opposite to the force. Due to the exponentially graded membrane stiffness, this effect is higher at the less stiffer (low frequency) side. Reduction of fluid coupling also shifts the position of maximal displacement to the low frequency side. The peak of the dotted graph in figure 2.9 is almost symmetric, as it is just the response of harmonic oscillators with varying resonance frequencies arranged along the cochlea.

Hydrodynamic coupling of distant parts of the cochlear partition is quantitatively studied using the model.

Hydrodynamic coupling is shown to sharpen the frequency response.

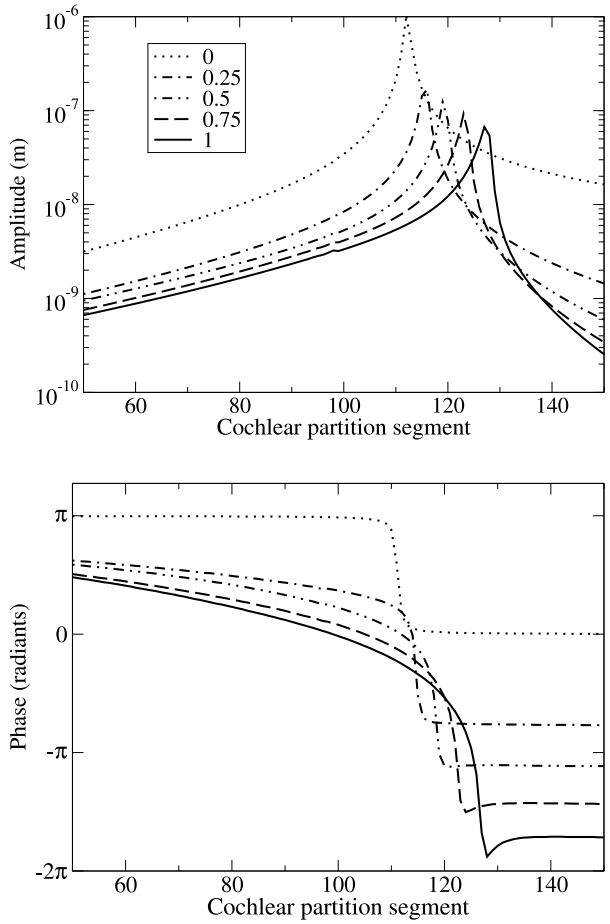

Figure 2.9: Upper part: Envelopes of cochlear partition amplitudes for pure tone stimulation. Stimulations with 1280 Hz for different values of hydrodynamic coupling c on a logarithmic scale. The absolute values of the slopes clearly increase with stepwise increasing coupling via the fluid. The sharpening takes place mostly at low frequencies (here the right-hand side). Amplification thereby decreases.
Lower part: The corresponding phases. Phases show, that in case of no hydrodynamic coupling ($c = 0$), there is no traveling wave as the phase is constant except for a small range near the resonance frequency. The stronger hydrodynamic coupling, the lower the velocity of the resulting traveling wave at the low frequency side as the slope of the phase becomes steeper.

2.4 Discussion

The main purpose of this chapter is to introduce a new base model of the cochlea, and accordingly some advantages and disadvantages are now pointed out.

Although a two-dimensional cochlear fluid is presumed, the equation of motion is one-dimensional. That is due to the proper positioning of the two arcs representing the oval window and the cochlear partition in the complex plane. Numerics can thus be implemented in a very straightforward way. In an comparative essay, Egbert de Boer [30, chap. 5] found numerical accuracy of the solution difficult to predict or to control for the three-dimensional case.

The cost of computation has decreased drastically in the years since the advent of two-dimensional cochlear models. Nevertheless, efficient computability is still important. Computing the cochlear response in real time, potentially with limited available computing power, and studying parameter dependency requires fast and simple models. Designing hardware implementations [31] requires fast estimates of implications of parameter modifications. In particular, it is not only single parameters that often have to be matched, but parameter functions, which makes the problem variational and computationally costly. In this way, the present model can turn out to be a useful tool supplementing existing one-dimensional models [6, 9, 32]. As it solves a simplified geometry exactly, it may also be used to evaluate finite element models. It can also serve as an initial point for further research, as it is easy to implement and to compute.

James Lighthill, former Lucasian Professor of Mathematics and member of the Royal Society, considered Allen's model [6], that was derived by the method of images, as the best among the two-dimensional theories [8]. That model, however, was impaired by

physical inconsistency and an unknown limit of a sum. In the present work application of conformal mapping allowed for the derivation of the fluid motion, governing the motion of the cochlear partition. The resulting equation is consistent and entirely analytic. Thus drawbacks of Allen's model could be overcome.

The model's simplicity also makes it useful as an example in lectures on hydrodynamics. Students may well benefit from this straightforward application of mathematics to biology.

In the present model the helicotrema is not neglected as for example in the models of Steele and Taber [14] or Lesser and Berkeley [7], since unfolding the cochlea makes the helicotrema part of the straight duct. The round window is consistently modeled as an open end, which is more realistic than a closed box [6].

But the present technique also has its shortcomings. Conformal mapping restricts all problems to two dimensions. Finding conformal mappings analytically for more realistic cochlea geometries leads to integrals that cannot by solved analytically anymore. The variation of the cochlea scalae, however, is of negligible importance as compared to those the cochlear partition [16]. It also seems unfeasible to include elastic properties of the round window. Yet, the displacement of the round window may well be small enough to neglect its elastic effect.

All in all, an analytical derivation of a cochlear equation of motion is achieved that opens up a gateway to efficiently handling a multitude of fascinating intrinsic dynamical patterns, such as what role hydrodynamic coupling effectively plays and how it can be treated analytically.

2.5 Outlook

As a side benefit, the model introduced allowed for the variation of the strength of fluid coupling of distant parts of the cochlear

partition independently of other parameters. This opened up a way to find out, whether the strength of interaction corresponds to an optimum. Hearing should be optimized for both selectivity concerning time and frequency. Supposedly there is some principle of uncertainty imposing restriction on optimality. Formally this means,

$$\Delta\omega\,\Delta t \leq \text{const}\,. \tag{2.22}$$

It would be interesting to know, how the product in equation (2.22) depends on hydrodynamic coupling c, the effect of which is shown in figure 2.9. To see, if the frequency selectivity increases with hydrodynamic coupling without a decrease in the temporal selectivity, is worth being found out. Furthermore it should be checked, if the systems performance gets worse when $c > 1$.

2.6 Appendix

2.6.1 Numerics

To solve the equation of motion (2.19) numerically, the cochlear partition is divided into N equally long elements of length $l = L/N$. The minimal coherence length, i.e. the distance over which a transversal section of the membrane will appear to move as a single structure, is about $120\,\mu$m [32]. Finer discretization would make the model less realistic. As others [33] did, it was chosen a total of $N = 300$ elements.

Each of those elements is indicated by j or k, such that $\eta = j\,l$ and $\eta_0 = k\,l$.

With η approaching η_0, $\Delta K^C\,(\eta, \eta_0)$ diverges. Thus one has to average the kernel by numerical integration in the neighborhood of

these singular points,

$$\Delta \bar{K}^C_{jk} := \frac{1}{l} \int\limits_{(k-1/2)\,l}^{(k+1/2)\,l} \Delta K^C\,(j\,l, \eta_0)\;\mathrm{d}\eta_0\,. \tag{2.23}$$

Correspondingly the averaged stapes-fluid interaction is defined by

$$\Delta \bar{Y}^S_j := \frac{1}{l} \int\limits_{(j-1/2)\,l}^{(j+1/2)\,l} \Delta Y^S(\eta_0)\,\mathrm{d}\eta_0\,. \tag{2.24}$$

To compute $\Delta \bar{Y}^S_j$ numerically using equation (2.18), which contains the term $\chi[\ln(\chi+1)-\ln(\chi-1)]$, this term was replaced by its limit 2 for $\chi > 10^6$ to avoid numerical instability. Upon introducing a mass matrix $\boldsymbol{M}$ with components

$$M_{jk} := \delta_{jk} m_k + \rho\, l\, b\, \Delta \bar{K}^C_{jk}\,, \tag{2.25}$$

and a vector $\boldsymbol{q}$ with components

$$q_j\left(\frac{\mathrm{d}\gamma_j}{\mathrm{d}t}\,(t)\,, \gamma_j\,(t)\,, t\right) := \rho\, b\, \Delta \bar{Y}^S_j \frac{\mathrm{d}v^S}{\mathrm{d}t}\,(t) - h\frac{\mathrm{d}\gamma_j}{\mathrm{d}t}\,(t) - k_j \gamma_j\,(t)\,, \tag{2.26}$$

one can reduce the discretized counterpart of equation (2.19)

$$\frac{\mathrm{d}^2\boldsymbol{\gamma}}{\mathrm{d}t^2}\,(t) = \boldsymbol{M}^{-1}\,\boldsymbol{q}\left(\frac{\mathrm{d}\boldsymbol{\gamma}}{\mathrm{d}t}\,(t)\,, \boldsymbol{\gamma}\,(t)\,, t\right)\,. \tag{2.27}$$

Together with the initial values

$$\frac{\mathrm{d}^2\boldsymbol{\gamma}}{\mathrm{d}t^2}\,(t_0) = \boldsymbol{M}^{-1}\boldsymbol{q}\left(\frac{\mathrm{d}\boldsymbol{\gamma}}{\mathrm{d}t}\,(t_0)\,, \boldsymbol{\gamma}\,(t_0)\,, t_0\right)\,, \tag{2.28a}$$

$$\frac{\mathrm{d}\boldsymbol{\gamma}}{\mathrm{d}t}\,(t_0) = 0\,, \tag{2.28b}$$

$$\boldsymbol{\gamma}\,(t_0) = 0\,, \tag{2.28c}$$

this results in an initial value problem that was solved by a second order Runge-Kutta method [34].

Each time step requires a multiplication of a vector of length N by the symmetric $N \times N$ matrix $\boldsymbol{M}^{-1}$ and therefore has the same computational complexity as all models that integrate equation (2.27). The condition number of $\boldsymbol{M}$ is approximately 498 and remains about the same even for larger N (525 for $N = 1000$, 534 for $N = 3000$, 537 for $N = 10000$, and 538 for $N = 30000$).

The parameters used for all graphs are listed in Table 2.1.

2.6.2 Cochlea parameters

Quantity	Value	Meaning
N	300	Number of cochlear elements
L	$33.5 \cdot 10^{-3}$m	Length of cochlear partition
ρ	10^3 kg/m^3	Density of cochlear fluid
H	10^{-3} m	Height of duct
b	$0.2 \cdot 10^{-3}$ m	Width of the elements
m_k	$1.7 \cdot 10^{-4} e^{85kL/N}$ kg/m	Mass* of k^{th} element
h_k	$0.165 - 0.1\, k/N$ kg/(ms)	Damping* of cochlear fluid
k_k	$2.8 \cdot 10^6 e^{-10.13\, k/N}$ kg/(ms^2)	Stiffness* of the k^{th} strip
a	10^{-9} m	Stapes amplitude
v^S	$a\omega \cos(\omega t)$	Stapes velocity

Table 2.1: COCHLEA PARAMETERS USED FOR SIMULATIONS. The parameters used in the simulations were taken from Mammano and Nobili [9], except for the width of the cochlear partition, which was taken to be constant, and the stiffness k, which was adapted to the frequency range of human hearing. The viscosity h is approximated by a linear function. The values could likewise be replaced by those of other species. Quantities marked with a star * are densities per length.

Chapter 3

Mammalian frequency-invariant sound localization

3.1 Introduction

The neuronal representation of the azimuth (angle in the horizontal plain) of a low-frequency (500 to 1500 Hz) sound source has been extensively studied across many mammalian and avian species [35, 36, 37, 38, 39, 40, 41, 42, 43]. There is general agreement, that the stimulus parameter that carries most of this positional information, is the interaural time difference (ITD), which is produced by the disparity of traveling times from the sound source to the two ears [44, 45, 46]. It is also unquestioned, that ITDs are neuronally represented via a firing rate pattern in populations of neurons in the brainstem. In mammals the underlying binaural coincidence detection takes place in the superior olivary complex (SOC) both in the medial superior olive (MSO) [35, 37, 41] and the low-frequency regions of the lateral superior olive [47]. In birds the binaural coincidence detection is performed in the Nucleus laminaris [38, 42], which is analogous to the MSO [48, 49]. The way that ITDs are exactly represented by the firing rates of neuron populations in the brainstem, is still a matter of debate and is presumed

The *interaural time difference* (ITD) is the difference in arrival time of a sound at the two ears. It is the main cue for localizing low-frequency sound.

The ITD is coded by the *firing rate* of neurons in the brainstem.

Coincidence Detection is a means by which neurons are not activated by single inputs, but mostly by the simultaneous activity of several inputs.

to vary across species [50, 51, 52]. Presently all quantitative coding theories have only considered ITD representations for stimuli with fixed spectral content [52, 53, 54]. Those theories showed, that the acuity, as found in psychophysical experiments, can be explained by the rate statistics of the best single neurons. The firing rates of ITD encoding neurons are, however, strongly altered by changes in stimulus frequency [36], as well as many other factors, such as sound level [35, 55], interaural level difference [56] and the presence and type of concurrent sounds [57, 58]. Taking into account additional stimulus dimensions complicates coding theories, because different activity patterns encode for the same ITD and thus the one-to-one relation between the firing rate of a single neuron and the stimulus ITD is lost.

Here a theory of ITD representation is developed that is invariant to one additional stimulus dimension: the frequency of a pure tone. Encoding by single cells are compared to two population encoding schemes here. It is found, that mutual information between single cell responses and stimulus ITD only roughly accounts for the observed variability of the response properties. The population patterns, however, are consistent with the idea of a two-channel code, in which the stimulus ITD is linearly represented by the difference of the overall activities in each hemisphere.

3.2 Results

The following analyses are based on recordings from the dorsal nucleus of the lateral lemniscus (DNLL) of Mongolian gerbils (Meriones unguiculatus). The DNLL is one stage downstream to the superior olivary complex and receives input from both the MSO and the lateral superior olive. Binaural DNLL responses have been shown to reflect the ITD sensitivities of SOC neurons well [2]. The data were obtained separately from $N = 153$ neurons from 41 an-

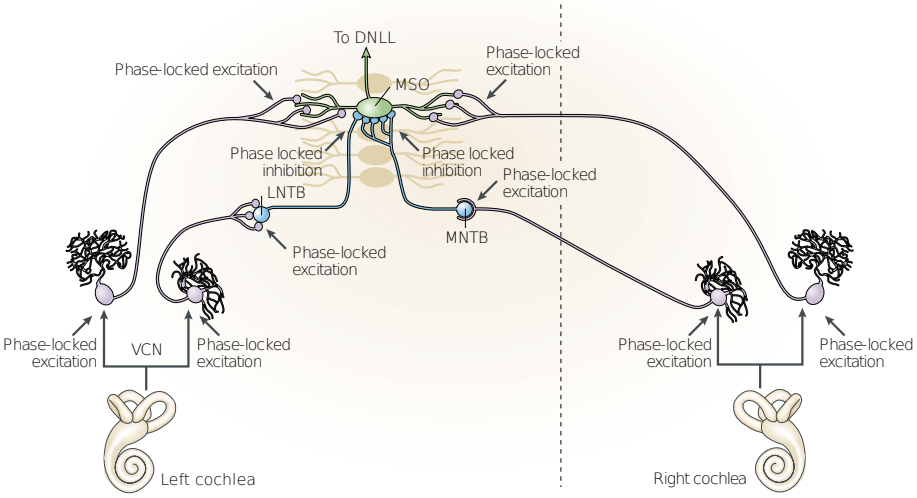

Figure 3.1: Mammalian ITD encoding system. Coincidence detection takes place in the medial superior olive (MSO), a structure of the auditory brainstem. Excitatory projections to the MSO originate from the left and right ventral cochlear nucleus (VCN). The contralateral medial nucleus of the trapezoid body (MNTB) and the ipsilateral lateral nucleus of the trapezoid body (LNTB) provide phase-locked inhibition to the ipsilateral MSO. MSO neurons extract the ITD from a comparison of their four inputs and project to the DNLL, the brainstem structure under consideration. (Image adapted from [49])

imals. Pure tone stimuli were applied with frequencies covering ±1/5 of an octave around the neuron's best frequency (BF). Stimuli were delivered binaurally with no interaural intensity difference and varying ITDs.

The *best frequency* (BF) is the frequency at which a neuron fires maximally.

The sensitivity of a single neuron to the ITD τ of the pure tone stimulus with frequency f is given by the tone delay function, which measures the neuron's firing rate as a function of the applied interaural phase difference (IPD) ϕ, which is the product of ITD and stimulus frequency $\phi = \tau \times f$. Tone delay functions in the brainstem strongly depend on the frequency of the stimulus (figure 3.2 A). Classically, this frequency dependence of the tone delay functions is quantified via the best IPD ϕ_{best}, at which the tone delay function of a neuron assumes its maximum. In the SOC and the DNLL, the best IPD of single neurons changes approximately linearly with frequency f ([37, 47, 2, 59, 60, 61] and figure 3.2 B),

The *interaural phase difference* (IPD) is the phase difference associated to an ITD and a certain frequency.

The *best IPD* is the interaural phase difference at which a neuron fires maximally.

In the mammalian brainstem the best IPD varies linearly with frequency. The linear variance is described by the *characteristic phase* (CP) and -*delay* (CD)

$$\phi_{\text{best}}(f) = \text{CP} + \text{CD}\, f \ . \tag{3.1}$$

The parameters describing this linear relationship are the characteristic phase (CP) and characteristic delay (CD). They are obtained by circular-linear regression between the circular variable ϕ_{best} and the linear variable f (see Appendix). For a pure delay line model as suggested by Jeffress [62], CD would be the difference of transmission delays from the two ears to a coincidence detector neuron, whereas CP should be zero (figure 3.3). This gets clear when reasoning as follows.

In the *Jeffress model* neurons fire maximally when the difference of axonal delays from both ears equals the ITD.

For the maximum response rate the best ITD exactly compensates for the difference of the neuronal delays, i.e. $\tau_{best} = \tau_{neuronal}$. By the definition of the best IPD, $\phi_{best} = \tau_{best} \times f$, direct proportionality of the best IPD and frequency $\phi_{best} = \tau_{neuronal} \times f =: CD \times f$ follows. Thus the offset termed CP must be zero.

The Jeffress model entails CPs being zero.

On the other hand, cells that receive inhibition from the contralateral ear and excitation from the ipsilateral ear would exhibit

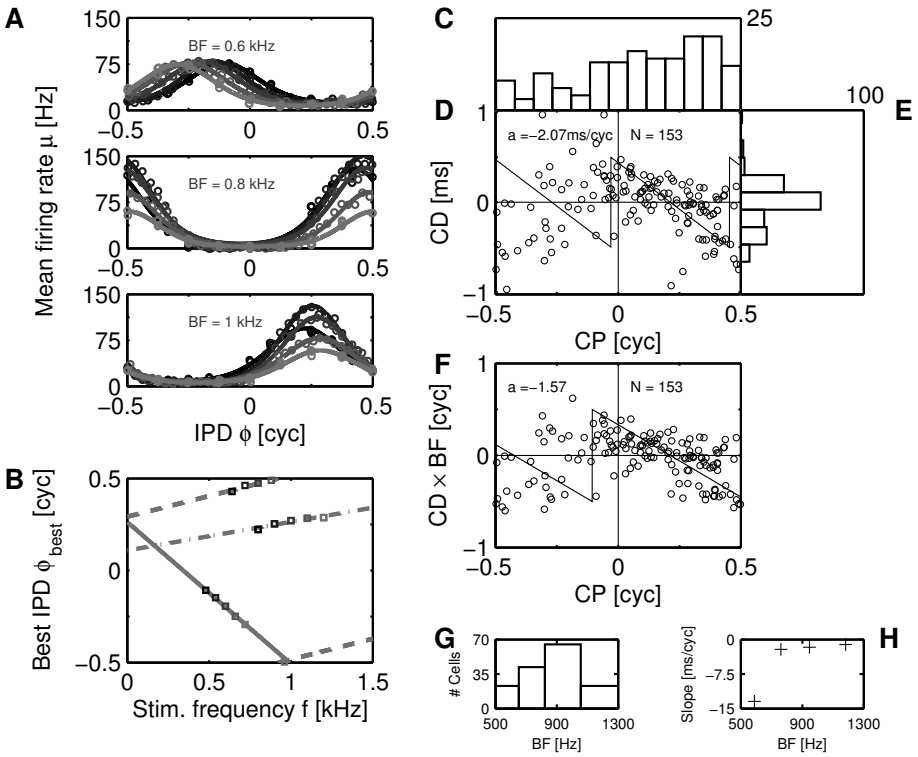

Figure 3.2: Frequency-variance of ITD sensitivity. (A) Tone delay functions for three exemplary DNLL neurons evoked by five stimulus frequencies (dark to light gray indicate low to high frequencies) centered at BF. Circles depict the means of measurements, the solid lines show a cyclic Gaussian fit (see Appendix). (B) Best IPD vs. stimulus frequency (phase-frequency curves) for the three neurons from A (corresponding to the three different line styles). Note, that the phase axis is cyclic. (C) Distribution of characteristic phases (CPs) for 153 DNLL neurons. (D) Best circular-linear fit to the distribution of CP and CD is depicted by the solid line (a: slope). (E) Distribution of CDs. (F) Correlation between CP and CD × BF. (G) Histogram of BFs. (H) Average slopes a of the CP, CD × BF distribution in the four frequency bands from G.

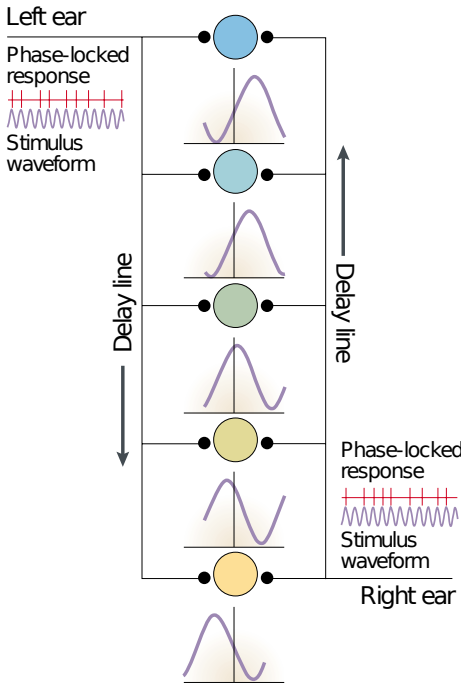

Figure 3.3: The Jeffress model. Neurons receive systematically delayed phase-locked excitatory inputs from both ears. The firing rate changes depending on both internal delays and the stimulus ITD. When the underlying neuronal delays exactly compensate for an ITD, the response rate of that neuron assumes its maximum. (Image adapted from [49])

CP=0.5. The distribution of CPs and CDs from the present data are quite different from these theoretical predictions. The CPs are distributed over the whole cycle with a bias towards positive phases (figure 3.2 C). The distribution of CDs peaks at zero and is skewed to negative CDs (figure 3.2 E). A circular-linear fit revealed a negative correlation between CDs and CPs with a slope of about 2 ms per cycle (mean resultant length $r = 0.51$, linear-circular correlation $\rho = 0.57$, $p < 8 \cdot 10^{-12}$ [63] (figure 3.2 D).

For the present data, CPs are broadly distributed and negatively correlated to CDs.

A slightly larger correlation ($r = 0.52$) was found between CP and the product CD $\times$ BF, which suggests a tonotopy in characteristic delays [64] (figure 3.2 F). A correlation between BF and CD was further corroborated by splitting up the data into four frequency bands with a width of 1/4 of an octave, and computing the circular linear fits in each of these bands (figure 3.2 G). The slopes of these fits correlate ($r = -0.98, p < 0.02$) with the mean BF in the bands, suggesting that large CDs predominantly occur in low-frequency bands (figure 3.2 H). Hence, for the further analysis the frequency-scaled parameter CD$\times$BF instead of CD was considered.

3.2.1 Single-cell mutual information

To understand how the observed distribution of CPs and CDs affects ITD coding, the mutual information between stimulus ITD τ and the corresponding firing rate r of a single cell,

$$I(r,\tau) = \sum_{r',\tau'} p_{r|\tau}(r'|\tau')\, p_\tau(\tau')\, \log_2\left(\frac{p_{r|\tau}(r'|\tau')}{p_r(r')}\right) \tag{3.2}$$

was calculated. The prior distribution p_τ of ITDs was obtained by assuming uniformly distributed dihedral angles (see Appendix). The prior depends on the inter-ear distance d that determines the maximal accessible ITD $\tau_{\max}$ and thus the physiological range of

The *Mutual Information* (MI) is a quantity measuring how much information a random variable conveys about another.

ITDs $[-\tau_{\max}, \tau_{\max}]$. The conditional distribution $p_{r|\tau}(r'|\tau')$ of observing a rate r' at a given ITD τ' is constructed from the recorded firing rates as follows. At first, the mean tone delay functions $\mu(\phi, f)$ are fit by cyclic Gaussians (figure 3.2 A). Then all recording conditions (ITD and stimulus frequency), that led to the same mean firing rate μ in one neuron, are pooled and neuron-specific Gaussian rate distributions $p_{r|\mu}(r'|\mu')$ are constructed by fitting the variance of the rate (figure 3.4 A and Appendix). From $p_{r|\mu}$, conditional distributions $p_{r|\tau,f}(r'|\tau', f') = p_{r|\mu}(r'|\mu(\tau'\, f'))$ of firing rates r' for given ITD τ' and stimulus frequency f' were constructed. The distributions $p_{r|\tau}(r'|\tau')$ were obtained by averaging over frequency, which reflects the assumption, that input frequencies are distributed uniformly under natural stimulus conditions (the differences for $1/f$ distributed frequencies are only minor) (figure 3.8). All present analyzes were done for neurons in the (best) frequency band between 800 Hz and 1000 Hz, in which there were the most cells ($N = 66$). This distinction between frequency bands was necessary, since the shape of the tone delay function in the physiological phase range strongly depended on the BF of the neuron. Nevertheless, the distributions for the other frequency bands was qualitatively similar, as far as one can tell from the limited sample sizes (figure 3.8).

Figure 3.4 B illustrates the mutual information for arbitrary pairs of CP and CD, using a phase delay function $\mu(\phi, f)$ with the average fit parameters of the population of neurons. Since the formalism is symmetric with respect to both hemispheres, the mutual information plot is mirror symmetric in the CP-CD $\times$ BF plane. The bright regions with high frequency-invariant information show distinctly negative slopes. The steepness of these slopes is roughly -1, i.e. CD $\times$ BF $\approx$ const. $-$ CP. All neurons along such a line thus have

the same best phase

$$\mathrm{BP} := \mathrm{CP} + \mathrm{CD} \times \mathrm{BF} \approx \text{const.}$$

In the case of figure 3.4 B, this constant best phase equals about 0.1 cycles.

To understand, what gives rise to high mutual information in these regions, examples were plotted for cells with high and low mutual information (figure 3.4 C). The "synthetic" cells with high mutual information have the steepest slopes of their rate response in the physiological range. The response functions of the cell with highest mutual information (cell 2) are very similar for all frequencies in the physiological range, which is indicative for the frequency invariance of the ITD representation for this single neuron. In general, however, the response of single neurons is not frequency invariant, even for those with high mutual information. The example cell in figure 3.4 C with low mutual information (cell 4) exhibits the peak in the physiological range.

Figure 3.4 B also shows, that the values of CP and CD $\times$ BF are not concentrated around the position of largest mutual information, nor do they follow exactly the line with slope -1. Some of the cells are even located at regions of the CP-CD $\times$ BF plane with very low mutual information. It therefore was quantified how much, if at all, the experimentally observed distribution of CPs and CDs provides an advantage for a frequency-invariant decoding of ITDs in terms of single-cell mutual information. Mutual information values were generated for a surrogate set of 1000 cells, which was obtained by shuffling the fit parameters of the mean tuning curves μ, while keeping CP and CD $\times$ BF constant. The mutual information of this control set was compared to that of a second surrogate set with shuffled CPs and CDs (figure 3.4 D). The gain in single-cell information due to the observed CP-CD distribution is rather small

The MI between firing rate and ITD, expressed in termes of the observed CP and CD, exceeds the MI of surrogate sets including that representing the Jeffress case.

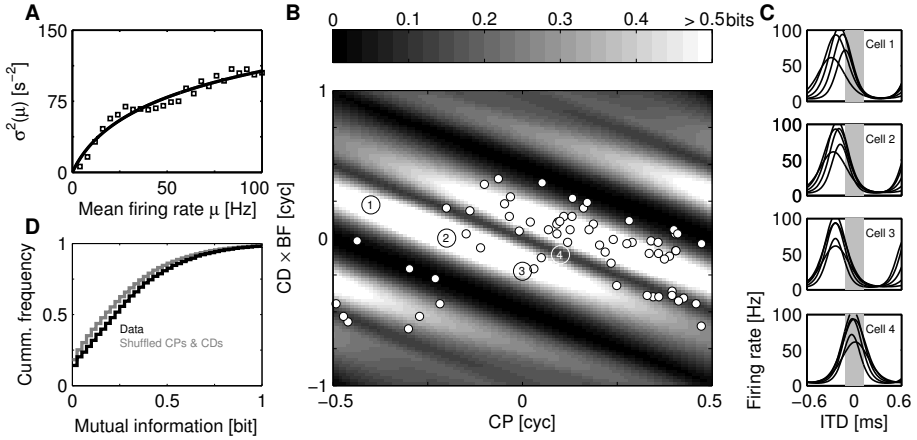

Figure 3.4: Rate statistics and mutual information. (A) Variance σ^2 of the rate distributions as a function of mean firing rate μ (squares averaged over all 153 neurons) and a logarithmic fit (solid line). For low rates the slope of the variance is consistent with a Poisson process (see Appendix). (B) Mutual information (MI; gray levels) as a function of CP and CD × BF for average fit parameters of the tone delay function in the best frequency band between 800 and 1000 Hz. Circles illustrate the distribution obtained from the DNLL population in this best frequency band. (C) Firing rate as a function of ITD for four exemplary combinations of CP and CD (large circles with numbers in B). Gray bars indicate the physiological range of ITDs. (D) Cumulative distributions of mutual information of the real CP-CD × BF pairs (black) and for 1000 repetitive shuffles of CP and CD × BF (gray).

(0.04 bits on average), but significant ($p < 10^{-202}$, Kolmogorov-Smirnoff test). Then all CPs were set to zero without changing the CDs, which would correspond to an idealized Jeffress-like situation with only delay lines and no additional phases. For such a setting one finds, that the mean mutual information would also become slightly worse by 0.015 bits ($p < 10^{-44}$, Kolmogorov-Smirnoff test), as compared to the measured distribution.

Next, one may want to know how much the single cell results are determined by the type of animal and the stimulus. Therefore it was studied, how the single-cell mutual information depends on inter-ear distance d and stimulus length T. At first, the influence of d was evaluated. From equation (4.1) one knows, that the inter-ear distance d influences the mutual information via the prior distribution p_τ of ITDs. Firing statistics $p_{r|\mu}$ determined from the gerbil DNLL recordings were used to make predictions about the population pattern of mutual information for hypothetical animals with larger inter-ear distances than that of the gerbil. The largest considered value gave rise to a maximal ITD $\tau_{\max} = 660\ \mu$s, which roughly corresponds to the situation in humans. For larger $\tau_{\max}$, the stripe-like organization was found to become less pronounced and the two clusters of high mutual information fused into one (figure 3.5 A). This fusion is associated with the maximum of the mutual information moving towards smaller characteristic phases. Thus it is concluded, that CPs different from zero are particularly useful for animals with small head size. For animals with larger heads, cells with large non-zero CPs still convey ITD information. However, they are less essential since ITD information is also available for small CPs.

Computing MI for different *physiological ranges*, that are confined by the corresponding maximum ITDs, allows for the prediction of CPs and CDs for various mammals.

MI suggests that CPs different from zero are particularly useful for small animals.

In a second analysis, predictions for reduced stimulus length were made in that only the activity, recorded during the initial interval of length T, was considered (figure 3.5 B). The stripe-like pattern in the mutual information profiles is present for every considered inter-

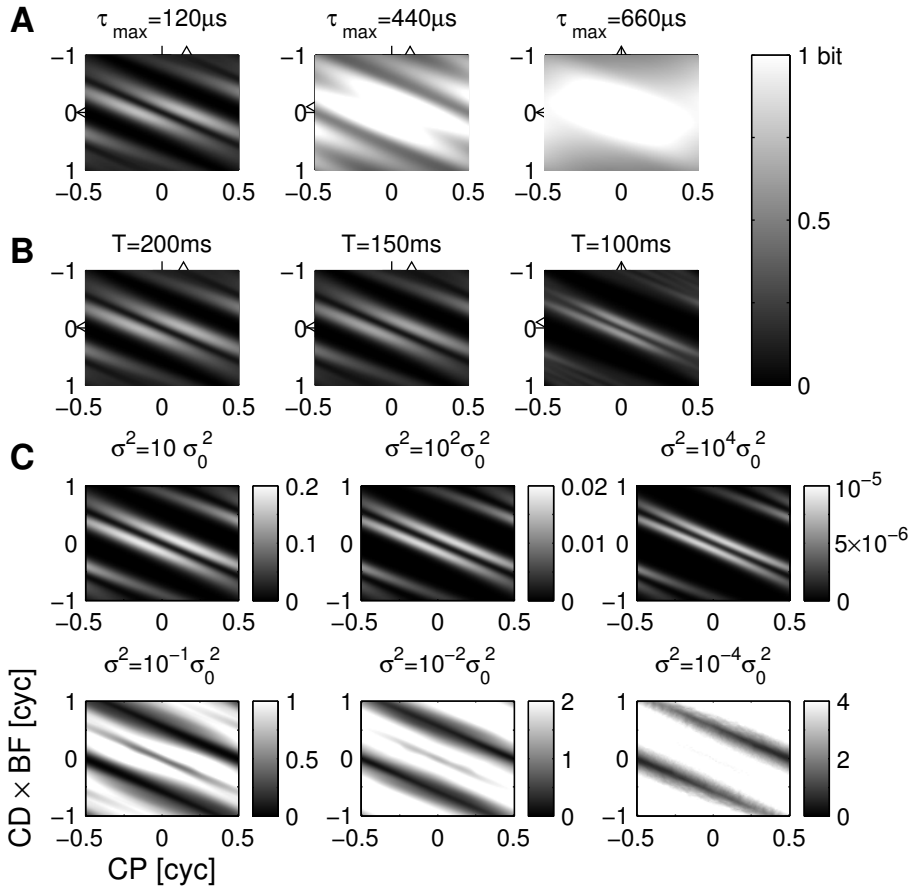

Figure 3.5: Parameter dependence of mutual information (MI). (A) MI as a function of CP and CD × BF for three different inter ear distances and the respective physiological ranges $[-\tau_{\max}, \tau_{\max}]$. The left plot is a copy of figure 3.4 D. Axis are the same for all subplots (see bottom left of C). The triangles on the top indicate the CP of maximum mutual information, the ticks on the top indicate CP=0. Triangles and ticks at the vertical axis indicate the analogous CD values. (B) MI for three different stimulus lengths. Again, the left plot corresponds to the default case from figure 3.4 D. Triangles follow the same convention as in A. The best phases (BP) are 0.16 cyc ($T = 200$ ms), 0.15 cyc ($T = 150$ ms), and 0.09 cyc ($T = 100$ ms). (C) MI for six different noise levels. Noise is defined as multiple of the variance σ_0^2 of the default case from figure 3.4 D. Note, that the MI is depicted with different gray scales (in bits).

val length T. With decreasing interval length, one finds a reduction in both the separation of the stripes with high mutual information and their thickness. In other words, a decrease in T makes the maximum mutual information move towards smaller CPs and the peaks of the phase delay function move into the physiological range.

MI suggests that CPs decrease as noise is increased or, equivalently, when the stimulus time T is decreased.

To find out, whether the changes induced by the reduction of T are due to different tone delay functions for onset and sustained firing, or mainly attributable to the increase of noise, also the mutual information for scaled noise levels was computed (figure 3.5 C). For artificially increased noise levels, the results were similar to those in figure 3.5 B for decreasing duration T; both separation and thickness of the stripes with high mutual information are reduced. However, for artificially decreased noise levels the stripes with high mutual information not only become thicker and fuse together, but also the maximum mutual information moves towards larger characteristic phases. As a consequence, regions with high mutual information also occur for both large positive CP and CD and very negative CP and CD (see Discussion).

To summarize, single cells in the DNLL do generally not exhibit frequency invariant ITD representations. However, the single cell mutual information suggests, that the observed distribution of CPs and CDs is particularly suited to conserve frequency-invariant ITD information. Thus it is proposed, that a frequency invariant ITD representation may be found by testing appropriate readout models for the population of DNLL responses.

3.2.2 Population codes

The single cell analysis has revealed two obvious problems: 1) Some of the cells have very low values of mutual information. 2) It is unclear, why not all of the cells cluster at the CP-CD position with maximal mutual information. To address these concerns, the cod-

Population coding is a means by which information is coded in a group of neurons.

ing capabilities of DNLL neurons were studied on the level of a population, using simulated firing rate patterns of $N = 66$ neurons in the frequency band between 800 and 1000 Hz for different ITDs and stimulus frequencies (figure 3.2 G). On the population level, where many neurons together encode a stimulus property, finding the most appropriate activity features is less obvious, particularly because responds across neurons is highly variable. It is shown, that the quality of the population code strongly depends on the assumption (or the model) of the population readout. It is argued, that invariances are useful constraints to identify proper population codes. Based on these ideas, it was suggested, that the representation of interaural time differences serves a two-channel code, in which the difference between the summed activities of the neurons in the two hemispheres exhibits an invariant and linear dependence on interaural time difference.

It is shown that the difference between the summed rates of the neuron populations of the two hemispheres serves an ITD coding which is linear and frequency-invariant.

First, rate patterns were used as input vectors to linear classifiers, that then produced a labeled line code with "grandmother neurons" that encode one specific azimuthal position (figure 3.6 A). For this purpose, linear support vector machines [65, 66] were trained in a one-vs.-one paradigm to classify the population patterns according to their underlying ITD into K categories (azimuth bins). The ITD resolution $\delta\tau = 2\tau_{\max}/K$ of the labeling scheme therefore is inversely proportional to the number of categories. As expected, the test error (predicted acuity) decreased and the training error increased with the number of training samples both saturating at a number of about $5\,N$ (figure 3.6 A). The test error converges to an acuity of about 17 μs, which is in agreement with the psychophysical acuity of gerbils of about 20 μs [67, 68]. This final acuity is reached at roughly $K = 9$ ITD bins.

To show, how much the negatively correlated distribution in the CP-CD $\times$ BF plane contributes to the test error, the CP values were shuffled again, however, no significant change of the test error

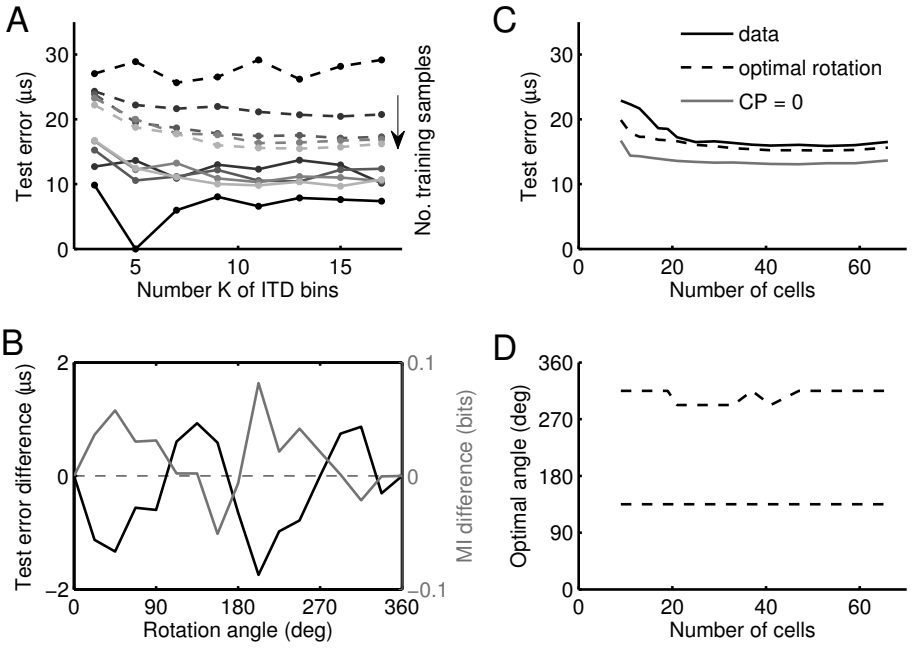

Figure 3.6: Linear separability of population patterns. (A) Test error as a function of the number K of classification bins for five different numbers of training samples ($N, 3\,N, 5\,N, 7\,N, 9\,N$ as indicated by gray level). Training errors are plotted as solid lines, test errors (localization acuity) are plotted as dashed lines. (B) Difference in test errors (black) and single-cell mutual information (gray) as a function of the rotation angle. Positive differences indicate, that the value obtained with the non-rotated CP-CD distribution is larger. For the linear classifiers the number of training samples was $5\,N$. (C) Test error as a function of the number of input neurons for the actually measured CP-CD distribution (solid line), for the optimal rotation angle (dashed line), and for CP set to zero (gray). (D) Optimal rotation angles at which the test error difference from B has local maximum.

was found. Therefore further manipulations in the CP-CD × BF space are carried out. First, all CPs were set to zero mimicking the distribution of the idealized Jeffress model. Surprisingly, this manipulation accounted for an improvement of about 3 μs of (root-mean-square) acuity ($p < 10^{-116}$, t-test for 150 repeats). The Jeffress model would thus be better suited than the actually observed DNLL population patterns, if neurons in higher-order nuclei acted as linear classifiers, or equivalently, if higher-order centers exhibited grand mother cells that fire specifically for small ITD intervals.

Second, the change of test error was monitored for rotated CP-CD × BF distributions that were constructed by rotating the CP-CD × BF position vectors of all single neurons by the same angle (figure 3.6 B). For rotation angles about 135° and 315°, the manipulated CP-CD distribution gave rise to about 1 μs improved acuity as compared to the unrotated case. These optimal angles also roughly coincide with the rotation angles, for which also the mean single-cell mutual information was found to be maximal. For none of the rotation angles, however, is the acuity as good as for the Jeffress-type scheme with CP=0.

A possible explanation for the above non-optimality of the population rate code is that a faithful frequency-invariant decoding of ITD could require less than the $N = 66$ neurons that were used as input to the linear classifier, i.e. the observed CP and CD values could be optimal for smaller subpopulations. Therefore classifiers were retrained with fewer input neurons. Figure 3.6 C depicts the mean acuity of the linear classifier as a function of the number of input units for both the actual and the optimally rotated CP-CD × BF distributions. For each number of input neurons, we chose the subset with highest values of single-cell mutual information. The acuity decreases with subset size, but quickly saturates at about 25 neurons. There it is only slightly worse ($\lessapprox 1$ μs) than the optimally rotated CP-CD × BF distribution. The optimal rotation

angles are independent of the subset size (figure 3.6 D). The acuity for the Jeffress case (CP=0), however, is always about 3 μs better.

Interestingly, no correlation between single cell mutual information and the weights of the classifiers (not shown) can be observed. This means, that only very few features of the population representation seem to be sufficient for the classifier to detect the right ITD, and the classifiers may learn different features of the population pattern for each frequency.

From the above findings it is firstly concluded, that the actually observed distribution of CPs and CDs is not optimal in terms of the readout acuity of linear classifiers and secondly, that only a small subset of cells would be sufficient to achieve best acuity.

As a second way to interpret the population rate pattern a bilateral difference model (or two-channel model) [68, 69] was considered, in which the total activity in one brain hemisphere is subtracted from that in the other hemisphere. Again, the focus was put on the frequency band between 800 and 1000 Hz, since there the distribution of best frequencies was pretty much flat and does not induce a sampling bias. Again firing rate patterns for different ITDs and stimulus frequencies were simulated, based on the rate distributions of the DNLL neurons. The bilateral (rate) difference signal D was computed as the mean firing rate in the population of simulated neurons, minus the mean rate for an identical population in the opposite hemisphere (with mirrored CP and CD). The relation between the stimulus ITD τ and the difference signal D is very well represented by a linear function (figure 3.7 A). The least squares fit $D = \alpha\,\tau$ thus provides a linear estimate of the stimulus ITD $\hat{\tau} = D/\alpha$. The test error between τ and its estimate $\hat{\tau}$ is largely independent of the stimulus frequency and ITD (figure 3.7 B, C).

Next the test error for a hypothetical population was recomputed with all neurons having the same optimal combination of CP and

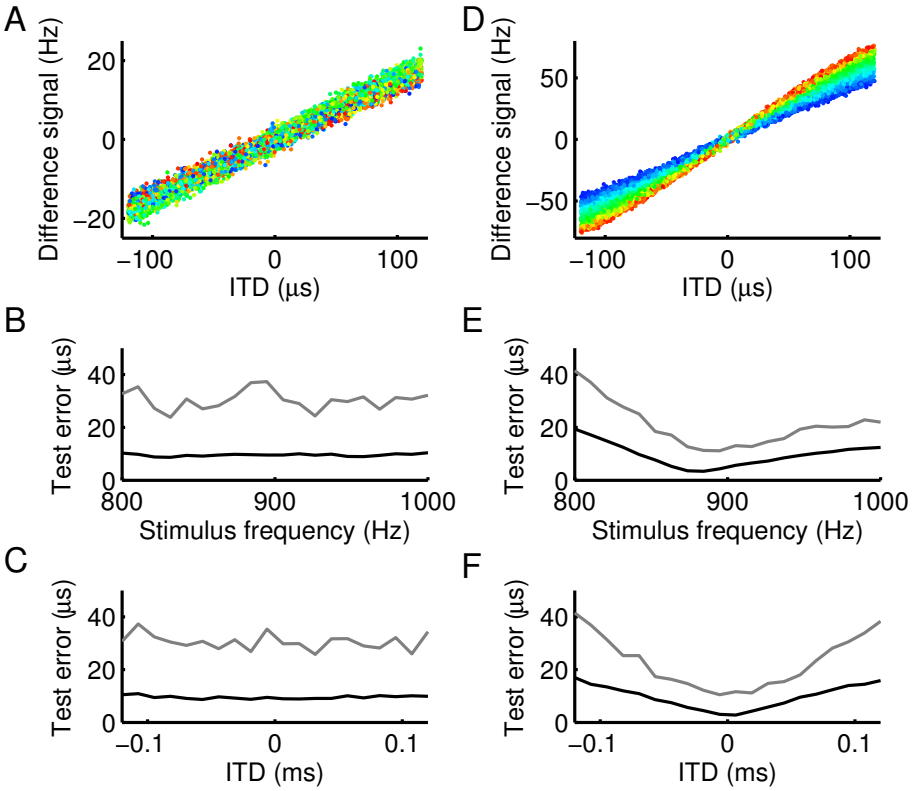

Figure 3.7: Bilateral difference coding. (A) Difference between the mean rate of the contralateral and the ipsilateral DNLL population. Colors indicate stimulus frequency from 800 Hz (blue) to 1000 Hz (red). (B) Test error as a function of frequency (black: root-mean-square error, gray: maximal error). (C) Test error as a function of of ITD (black: root-mean-square error, gray: maximal error). (D-F) Same as A-C where all neurons are simulated using the combination of CP and CD with highest mutual information.

CD, at which the mean mutual information from figure 3.4 D is maximal. The relation between difference signal and ITD is no longer linear and clearly depends on the stimulus frequency (figure 3.7 D). As a result, also the test error depends non-monotonically on frequency with a minimum at the center frequency of the band (figure 3.7 E). The observed variability in CP and CD thus is responsible for the frequency-invariant linear relation between ITD and the difference signal. Moreover, this linearity is robust with respect to a small jitter in the CD and CP values and, hence, this property does not depend on the exact distributions measured (figure 3.8). Figure 3.9 also shows, that a similar linear difference signal is obtained from the smaller subset ($N = 41$) of units measured with best frequencies between 600 and 800 Hz, indicating, that the linear readout is not a specialty of the considered best frequency band.

As before, the test error for manipulated cell characteristics was determined, i.e. rotations in CP-CD $\times$ BF space and CPs were set to zero (not shown). In all cases, the original distribution of CP and CD was found to clearly provide the best acuity of about 10 μs. Specifically for the Jeffress-like situation (CP=0), one finds a a-mean-square test error of 120 μs, i.e., the maximal ITD.

To conclude, for hemispheric rate difference representation the experimentally observed distribution of CP and CD $\times$ BF is more suitable in terms of test error and frequency invariance, than all artificial ones tested.

3.3 Discussion

Responses of ITD-sensitive neurons in the DNLL of gerbils change with the frequency of a pure tone stimulus, similar to all other ITD sensitive neurons in the brainstem [2]. Here, this frequency-dependent modulation was evaluated in terms of its influence on

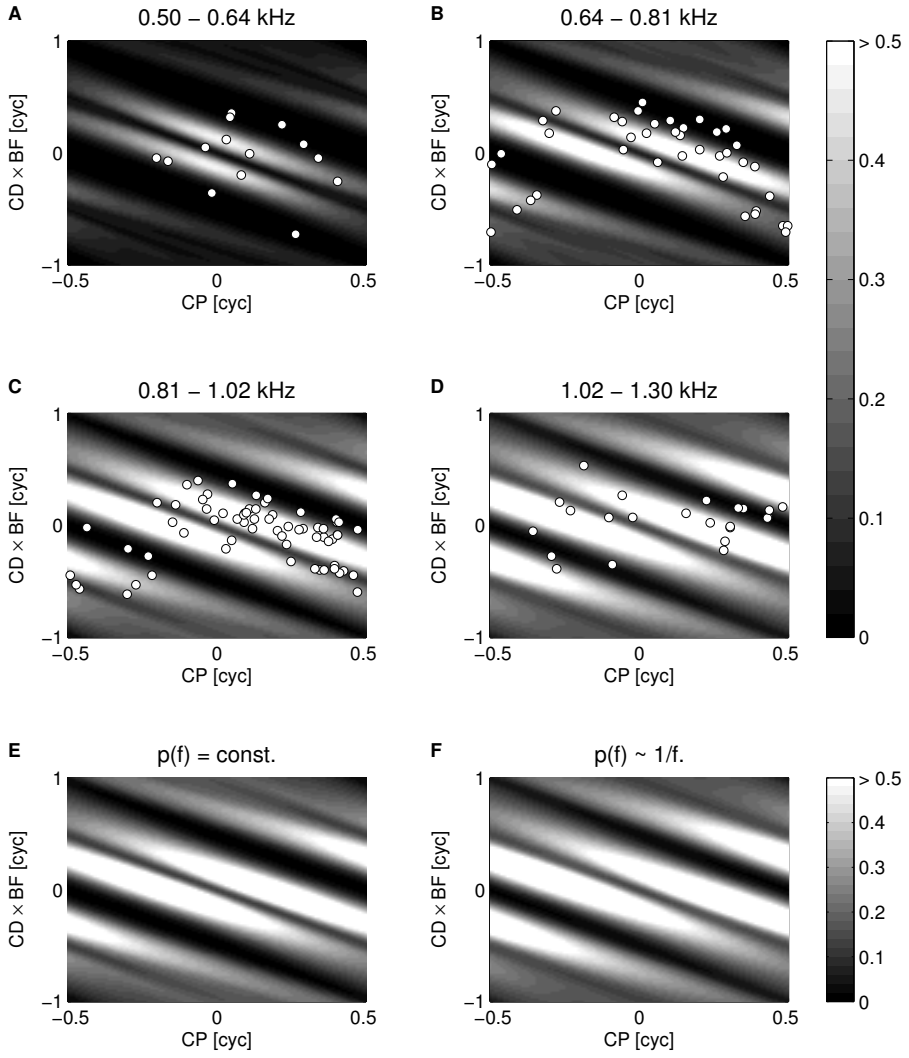

Figure 3.8: Robustness of single cell mutual information. (A-D) Single cell mutual information for different best frequencies. White circles represent measured CP, CD × BF values for the cells in the respective best frequency band. (E,F) Single cell mutual information for uniform (E) and power-law (F) frequency distribution (E is the same gray level plot as C).

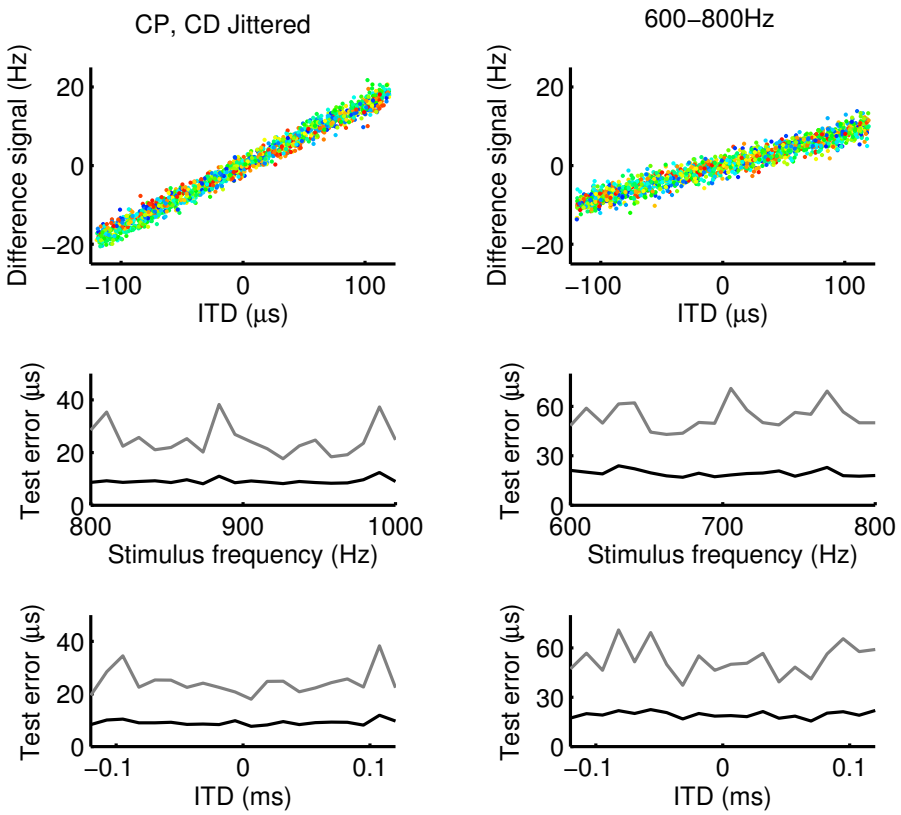

Figure 3.9: Robustness of linear rate difference signal. Left column: Linear rate difference code for a model population, at which the CP, CD × BF values are jittered around the measured values according to a Gaussian distributions with standard deviation 0.023 cyc. for CP and 0.22 cyc. for CD × BF (figure 3.10). Right column: Linear rate difference code for the 41 cells in the (best) frequency band between 600 and 800 Hz. The arrangement of the sub panels is identical to those in (figure 3.7).

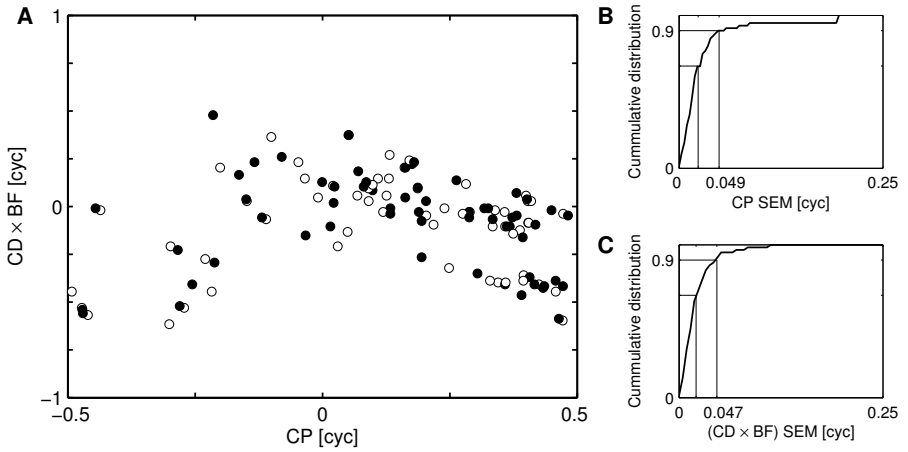

Figure 3.10: Robustness of CP, CD estimate. (A) Measured distribution (white) and one example of a surrogate distribution (black) obtained by randomly generating spike counts from a Gaussian distribution with cell-specific mean and variance. (B, C) Four surrogate spike counts (like in A) were generated for each cell and used to derive cell-wise standard errors of the mean (SEM) for CP and CD × BF. (B) Cumulative distribution of SEM for CP ($N = 66$ cells). Vertical lines indicate the SEM values of about 0.023 cyc. and 0.049 cyc. at the 67% and 90% quantile, respectively. (C) Same as B for CD × BF, with SEM values 0.022 cyc. and 0.047 cyc. at the 67% and 90% quantiles.

the encoding of ITD by firing rate patterns of the neuronal population. For the 153 recorded cells the frequency dependence was characterized by the two parameters characteristic phase (CP) and characteristic delay (CD) [36]. It was found, that the two parameters are significantly negatively correlated, as has also been reported for the mid brain and DNLL of guinea pigs [64, 70], although there DNLL data did not reveal negative CDs. Also consistent with these and several other studies in various binaural brainstem nuclei and animals, it was found that CPs are broadly distributed over almost the whole phase cycle [37, 40, 61, 71].

Analysis of single-cell mutual information revealed, that the observed distribution of CPs and CDs performs slightly better than a distribution with shuffled CPs and CDs. Furthermore, the single-cell mutual information strongly depends on the noise level. It was found, that for high noise levels, peak-based codes are advantageous in terms of mutual information. For low and moderate noise levels mixed coding schemes were found to be viable: Both slopes and peaks can be used to extract information and should be located in the physiological range. These results are consistent with theoretical work comparing slope and peak-based coding schemes [72, 73]. There it is generally shown, that for high noise levels, strong signal changes are preferred and thus binary-like (i.e. peak-based) codes are beneficial. For low noise, slope-based codes are preferred since only then can continuous rate changes be sampled well enough.

The statistical model allows derivation of hypothetical distributions of CP and CD for different head sizes. As expected, mutual information grows with increasing inter-ear distance. Also the regions of highest mutual information move towards smaller CPs, when the inter-ear distance was increased. Interestingly, this effect corresponds well to the finding, that for large mammals the medial superior olive (MSO; with most CPs between 0 and 0.25 cycles) is generally larger than for smaller mammals [74].

An increase in the inter-ear distance can alternatively be interpreted as an increase of best frequency. In both cases, tone delay functions with peaks in the physiological range exhibit increased mutual information. With this interpretation, one can also assess the situation when phase-locking is present up to several kHz, as found in the barn owl [38, 75]. There, as well as for a large head diameter, the two regions of high mutual information merge into one cluster centered about CP=CD=0. As a consequence, a Jeffress-like coding strategy with CP=0 would be sufficient for achieving high single-cell mutual information.

The variability of phase delay functions in the DNLL provides the basis for a frequency-invariant population representation of ITDs. Both of two readout strategies, a linear classifier and a bilateral rate difference signal (two channel code), are found to explain a coding acuity of down to 10 μs. For the linear classifier, however, the observed distribution in CP-CD$\times$BF space with BP clustered about 0.1 cycles is suboptimal in that a Jeffress-type representation with CP=0 would account for a better acuity. For the bilateral difference code the observed distribution of CPs and CDs seems appropriate, particularly because of the linearity and the frequency invariance of the difference signal. There a Jeffress-like representation would yield a much lower acuity.

The behavioral acuity of gerbils at mid line ($\varphi = 0$) has been estimated as 20 μs [67, 68] and thus is worse than the acuity of about 10 μs derived from the bilateral difference model. Such hyper acuity of the estimator is not surprising, as the relative noise decreases with the size of the population. In general, hyper acuity has two possible explanations. First, it may hint at several noisy downstream readout stations before the localization signal is translated to a behavioral response. As a second possibility, however, it could also hint at hidden stimulus dimensions that are not taken into account by the decoding model. As for the frequency depen-

dence discussed in this chapter, one could also ask for a code to be invariant with respect to intensity, background noise and so forth. Each of these additional dimensions, hence, reduces the predictive value of single neurons. The real psychophysical acuity should then be achieved by a decoding model that takes into account all possible invariances assuming no further noise in the readout.

Another possible discrepancy to psychophysical data is, that the acuity of the bilateral rate difference model is independent of stimulus ITD. In humans, the minimal audible angle at lateral (azimuth $\varphi = 90°$) positions is up to 10 times worse than at frontal positions ($\varphi = 0°$) [76]. However, the transformation from angle to ITD only accounts for a factor of about 2 (see Appendix). Indeed, the psychophysical ITD resolution for low-frequency pure tones is about 2 to 5 times worse for lateral positions as for frontal ones [76]. In gerbils, localization acuity has not yet been determined at locations different from mid line. However, the bilateral difference model predicts, that in gerbils the just noticeable ITD difference is independent of azimuth and conversely the acuity in terms of azimuthal angle should be about 2 times worse for lateral positions than at mid line. This feature could be a specialty of animals with small head size, because if the inter-ear distance gets larger, more peaks of the phase delay functions move into the physiological range and impair decoding via a difference rate particularly for more lateral positions.

Non-zero CPs are most often thought to originate in the lateral superior olive where neurons receive inhibition from contralateral and excitation from ipsilateral. The combination of these antiphasic signals is able to explain CPs around 0.5 and low CDs. Such cells are generally called troughers. For neurons that receive bilateral excitation (as in the MSO), CPs different from zero still pose a major problem for mechanistic models of ITD sensitivity as the physiological mechanisms that give rise to them are not fully

identified yet. The classical Jeffress model [62], in which the best ITD is solely determined by temporal latency differences, predicts constant CP=0. Cells with small CPs are generally called peakers. There are several candidate models for non-zero CPs in binaurally excited neurons. 1) Ipsi- and contralateral input fibers might have mismatched center frequencies and thus a mismatch of phases might be induced by the preprocessing of different cochlear filters [77]. 2) Morphological asymmetries [78] of the coincidence detecting neuron can induce distinct temporal filtering of the ipsi- and contralateral inputs. 3) Phase-locked inhibition [41, 59, 79, 80] that differs between ipsi- and contralateral input can induce asymmetric phase shifts. 4) Phase disparities may be a direct consequence of asymmetries in the ipsi- and contralateral excitatory synaptic kinetics [81]. The present study shows, that generating specific CPs may not just be an epiphenomenon of the physiological mechanisms that underlie ITD-sensitive responses in the brainstem, but may be required for an optimal neuronal representation of ITD. Thus the physiological mechanisms underlying ITD sensitivity should allow the deliberate tuning of CPs, which argues against hard-wired solutions as (1) and (2) and favors synaptic mechanisms like (3) and (4).

A problem in the interpretation of the present data is, that the DNLL is not a primary nucleus in which the ITD-sensitive responses are computed. The ITD representation in the DNLL might already be imposed by secondary processing steps. Instead one would rather want to compare population responses in the MSO (for low CPs) and the low-frequency region of the lateral superior olive (for high CPs). Single units in the MSO are, however, difficult to record from. Data from a few tens of gerbil MSO units also shows negatively correlated CP and CD with a broad distribution of CPs (unpublished observation about data from [60]). The DNLL, however, is a particularly good place to study ITD population codes, since it is much easier to record from than the MSO, and, more-

over, it is the first station in which genuine ITD-sensitive responses from MSO (peakers) and lateral superior olive (troughers) are combined [2]. The only major computation occurring at the synapses from the SOC to the DNLL seems to be noise reduction [55].

Most theoretical analyzes of neuronal representations deal with only one or two stimulus dimensions, as e.g. the frequency of a tone or the loudness of a sound. In the example discussed in the present chapter, the two stimulus dimensions ITD and frequency are both physically and statistically independent, since sound position and sound spectrum are generally unrelated. Here it was shown, that considering population responses across an invariant dimension (frequency) of the stimulus not only allows the assessment of the neuronal population representation in terms of coding acuity, but also allows to evaluate, how different hypothetical invariant read-out strategies fit to the population representation.

3.4 Outlook

The present chapter deals with frequency-invariant neuronal representations of the azimuth of a single source emitting a pure tone. Future effort should target at putting additional dimensions like elevation, loudness or additional sound sources into an invariant framework. Furthermore, frequency-invariant representations ought to be studied for different species, which is carried out for the barn owl in the next chapter.

3.5 Appendix

3.5.1 Stimuli

The standard setting was stimulus duration of 200 ms plus cosine rise/fall times of 5 ms, presented at a repetition rate of 2 Hz. To

search for acoustically evoked responses, binaurally uncorrelated noise stimuli were delivered. When a neuron was encountered, first its best frequency (BF) and absolute threshold was determined using binaurally identical pure tone stimulation. The frequency, that elicited responses at the lowest sound intensity, was defined as BF, the lowest sound intensity evoking a noticeable response at BF as threshold. Sensitivity to interaural time differences (ITDs) was primarily assessed by presenting a matrix of pure-tone stimuli with varying ITDs and stimulus frequencies 20 dB above threshold. Different ITDs were presented over a range equivalent to at least one cycle of the stimulus frequency f. ITD sensitivity was tested for 5 frequencies around BF (covering $\pm 1/5$ of an octave) and an interaural intensity difference of 0 dB. Each stimulus was repeated at least three times.

3.5.2 Tone delay functions

Tone delay functions describe the firing rate of a neuron as a function of the stimulus ITD for a fixed stimulus frequency f. In this chapter, for the purpose of a simpler notation, tone delay functions are considered to depend on the interaural phase difference (IPD) $\phi := f \times \mathrm{ITD}$. The rates were averaged over all repetitions of the respective pure tone stimulus and fit by the cyclic Gaussian

$$\mu_f(\phi) = \mathrm{a}_f \exp\left[\beta_f \left(\cos[\pi(\phi_f - \phi)]^2 - 1\right)\right] + \mathrm{b}_f \ , \tag{3.3}$$

providing four fit parameters a_f, b_f, β_f, and ϕ_f. The parameter ϕ_f accounts for the IPD, at which the fit has its maximum value and is called the best IPD ϕ_{best}. Note, that also negative values for the best phase can occur and are kept as such in the present analysis.

3.5.3 Circular-linear regression

The best IPD ϕ_{best}, as a function of the frequency f of the pure tone stimulus, is called phase-frequency curve. It relates a circular (phase) variable, ϕ_{best} to a linear variable f. This relation is used to derive single cell characteristic phase (CP) and characteristic delay (CD) using Equation (3.1). Quantification of correlations between CP and CD in the population of cells also requires to assess the relation between a circular variable (CP) and a linear variable (CD) (figure 3.2 E). To fit linear relations between pairs of measurements $\{(\phi_1, x_1), \ldots, (\phi_N, x_N)\}$, in which the dependent variable ϕ is a circular quantity (e.g. CP or IPD), and the independent variable x is linear (e.g. CD or frequency), the approach by Schmidt et al. (2009) [82] is followed: Assuming the linear model $\phi(x) = A\,x + \Phi_0$, one computes the mean resultant length r of the circular errors between the measurements ϕ_n and the model $\phi(x_n)$:

$$r(A) = \left| \sum_{n=1}^{N} \mathrm{e}^{i(\phi_n - A\,x_n - \Phi_0)} \right| \ . \tag{3.4}$$

If the model exactly fit the data, r would take the maximal value N. Since in Equation (3.4) the dependence on the phase offset parameter Φ_0 cancels out, the slope parameter A can be obtained from one-dimensional numerical maximization of $r(A)$. For the resulting optimal slope A, the offset Φ_0 then follows from maximizing

$$q(\Phi_0) = \sum_n \cos(\phi_n - A\,x_n - \Phi_0) \ ,$$

which accounts for maximizing the overlap between the data cloud and the linear fit on the surface of a cylinder. Maximization of q was already suggested by Agapiou and Mc Alpine (2008) [64] for fitting CP. Significance and correlation coefficients of circular linear fits was evaluated using the Matlab package circstat [63].

3.5.4 Prior distribution

To obtain the mutual information between stimulus position and single cell firing rate according to equation (4.1), a model for the probability distribution $p_\varphi(\varphi')$ of the interaural angles of the sound sources is required.

A uniform distribution of the dihedral angles of the sound sources corresponds to a distribution $p_\varphi(\varphi') \propto \cos(\varphi')$ of interaural angles φ on the great circle defined by the sound source elevation. For zero elevation, φ is equivalent to the azimuth. Following Blauert [46], the interaural angle is mapped to the ITD τ via

$$\tau = \frac{d}{2\,c}\left(\varphi + \sin\varphi\right) . \tag{3.5}$$

Unless otherwise mentioned, an inter-ear distance of $d = 32$ mm is used for the gerbil. Together with the speed of airborne sound $c = 340$ m/s, this leads to a physiological range of ITDs of 120 μs. The prior distribution of ITDs is then obtained as

$$p_\tau(\tau) = p_\varphi(\varphi)\,\frac{\mathrm{d}\varphi}{\mathrm{d}\tau} \propto \frac{\cos\varphi(\tau)}{1+\cos\varphi(\tau)}$$

where $\varphi(\tau)$ is the numerical inverse of equation (3.5).

3.5.5 Rate distributions

To obtain the mutual information between firing rate and stimulus position following the procedure described after equation (4.1), an estimate for the conditional probability distribution $p_{r|\mu}$ of observing a firing rate r, given a stimulus that evoked mean response rate μ, is required. The corresponding rate histograms were constructed cell-wise for each mean firing rate μ and fit by a Gaussian (figure 3.4 B),

$$p_{r|\mu}\left(r|\mu\right) \propto \theta\left(r\right)\exp\left(-\frac{(r-\mu)^2}{2\,\mathrm{var}(r)}\right) . \tag{3.6}$$

Here, the step function $\theta(r)$ is included to clip negative firing rates, it equals 1 for $r \geq 0$ and zero for $r < 0$. The variance $\mathrm{var}(r)$ (pooled over over all cells) could be fit by a logarithmic relation

$$\mathrm{var}(r) = v_0 \, \ln(1 + r/\rho) \; .$$

For a stimulus length of $T = 200$ ms, the fit parameters were $v_0 = 46.2$ Hz^2 and $\rho = 11$ Hz. For small rates the logarithm can be expanded and leads to the approximate relation $\mathrm{var}(r) \approx v_0/\rho \, r$. The variance of the spike count $s = r\,T$ thus becomes $\mathrm{var}(s) = 1.05\,s$, which is Poissonian to an excellent approximation. For large rates the variance of the spike count increases strongly sub-linear, meaning, that DNLL cells encode much more faithfully than Poisson at high rates [55].

3.5.6 Linear classifiers

To evaluate the possibility of a population representation of ITDs via grandmother neurons, K categories (labels) were defined, which correspond to ITDs being in intervals of size $\delta\tau = 2\,\tau_{\max}/K$. Grandmother neurons are assumed to respond to ITDs from only one of these bins. Using the machine learning package Shogun [66], the weights $w_1 \ldots, w_{66}$ of linear decision variables

$$h(\{r_1, \ldots, r_{66}\}) = \sum_{n=1}^{66} r_n \, w_n - w_0$$

were learned using input data $\{r_1, \ldots, r_{66}\}$ generated by the stochastic model that was fit to the DNLL rate responses. Training was done in a one-vs.-one mode, i.e. for each pair of bins a support vector machine (SVM) was trained to distinguish between those two categories. Thus, for K ITD bins a total of $K\,(K-1)/2$ SVMs had to be trained. The estimated ITD bin $\hat{k} \in \{0, ..., K-1\}$ of the pattern is the one, which has the most votes from the $(K-1)$ SVMs,

that were trained to classify it. The grandmother neurons are thus assumed to implement a winner-take-all based on the number of votes. The (root mean square) test error on a set of M test inputs is computed as

$$\mathcal{E} = \left(M^{-1} \sum_{m=1}^{M} (-\tau_{\max} + \hat{k}_m \, \delta\tau - \tau_m)^2 \right)^{\frac{1}{2}} .$$

Chapter 4

Avian frequency-invariant sound localization

4.1 Introduction

The neuronal circuits that encode ITDs in birds and mammals implement different solutions to the same problem (figures 4.1 and 3.1).

Coincidence detector neurons have been found in the brainstem of both mammals and birds [48]. In birds, the system encoding the interaural time difference (ITD) is thought to be similar to what Jeffress suggested [49] (figure 3.3). It was found particularly in barn owls [38], where axons provide systematic internal delays to coincidence detector neurons (figure 4.2 A). Depending on how internal delays from the left and right ear to a coincidence detector neuron compensate for the corresponding ITD, firing rate changes (figure 4.2 B). When the underlying internal delays exactly compensate for an ITD, the response rate of this neuron assumes its maximum. In birds, the coincidence detection is performed in the Nucleus laminaris (NL), which receives excitatory input from both ears [38, 42] (figure 4.1).

The NL is analogous to the medial superior olive (MSO) of mammals [48, 49]. The gerbil MSO receives excitatory as well as inhibitory inputs from both ears (figure 4.2 D). Inhibitory input adjusts the response of MSO cells to exhibit the highest variability

in the physiological range (figure 4.2 C). Therefore, maximal responses are found outside of the physiological relevant range. In the opposite MSO, responses look like mirror images. This distribution suggests, that the ITD is coded by the difference of both MSO activities, rather than by the activity of only one MSO [69, 68]. The dorsal nucleus of the lateral lemniscus (DNLL) adopts ITD sensitivity from the MSO. In the previous chapter, the possibility of DNLL structures to exhibit a difference code was shown [3]. The maximal response to ITDs of neurons in the NL equally distribute across the physiological range [83]. Neurons of the NL pass on ITD sensitivity to the forebrain. This chapter includes ITD coding of forebrain neurons, examines the possibility of a difference code in the forebrain and contains further comparisons to mammalian ITD encoding.

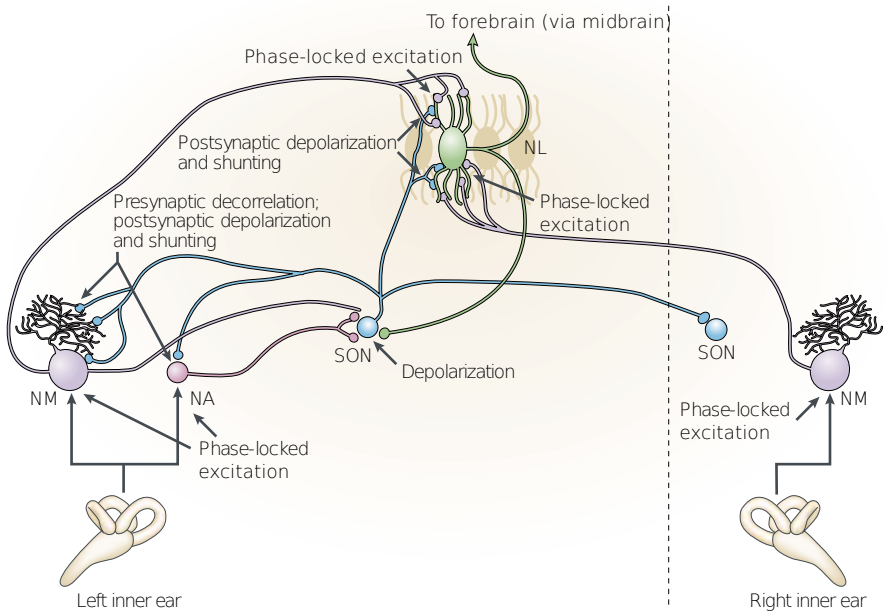

Figure 4.1: Avian ITD encoding system. The nucleus laminaris (NL) is the avian counterpart of the mammalian MSO. Neurons of the NL receive phase-locked excitation from the nucleus magnocellularis (NM) of both hemifields. NL neurons receive inhibition from the superior olivary nucleus (SON), which in turn receives input from NM and the nucleus angularis (NA) and inhibitory feedback from the NL itself. This inhibition provides a differential gain control for the ITD detector mechanism [49] (image adapted from [49]).

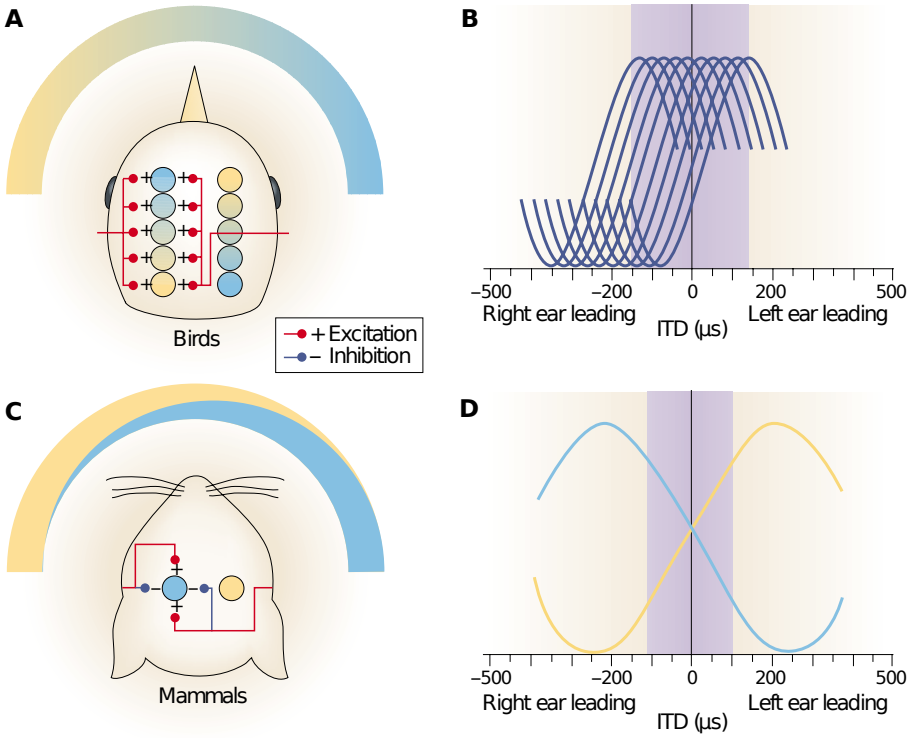

Figure 4.2: Avian and mammalian ITD coding. (A) Structures in the bird's nucleus laminaris (NL) come close to the delay line arrangement as suggested by Jeffress. Neurons receive systematically delayed excitatory inputs from both ears (here only input to the left hemifield is shown). (B) Tone delay functions are found to be equally distributed across the physiological range (shaded area). (C) The mammalian medial superior olive (MSO), which is analogous to the NL, receives excitatory and inhibitory input from both ears. (D) Tone delay functions are adjusted to exhibit highest variability in the physiological range (shaded area). Tone delay functions of the other hemifield look like mirror images. An ITD is represented by the difference of the activities of the two MSOs (yellow and blue half curve). (Image adapted from [49])

4.2 Results

The following analyses are based on recordings from the auditory forebrain (Prosencephalon) of the barn owl (Tyto alba). Auditory forebrain neurons adopt ITD sensitivity from the auditory brainstem neurons of the NL that compare phase locked inputs from both ears. The recordings were gathered from $N = 113$ neurons from eight owls. ITDs τ varied in steps of 30 μs within the physiological range, which covers the range between $-\tau_{\max}$ and $\tau_{\max} = 270\,\mu$s for the barn owl. Pure tone stimuli were applied with frequencies f between ~ 2300 and ~ 8300 Hz (see Appendix). For the sake of a better comparison, only the 28 (of 113) neurons that were stimulated with (at least) all of the frequencies 3333, 4167, 4762, 5555, 6666 and 8333 Hz were analyzed.

Responses of the single cells determine tone delay functions that measure the trial-averaged firing rate of a neuron as a function of ITD $\mu(\tau)$ or, alternatively, as a function of the interaural phase difference (IPD) ϕ (see Appendix). Tone delay functions are fit by the first component of their Fourier series (see Appendix). They strongly depend on the frequency of the stimulus (figure 4.3 A). This frequency dependence of the tone delay functions is typically quantified via the best IPD ϕ_{best}, at which the tone delay function assumes its global maximum.

In case of the gerbil DNLL, the best IPD of neurons changes approximately linearly with frequency ([37, 47, 2, 59, 60, 61] (see previous chapter). This linear dependence is characterized by the characteristic phase (CP) and the characteristic delay (CD) the introduction of which allowed for an frequency-invariant interpretation of ITD coding. For barn owl forebrain neurons, no such linear dependence of best IPD on frequency could be found for sufficiently many cells (figure 4.3 B). The Jeffress model entails direct proportionality of best IPD and frequency. Therefore the Jeffress

Unlike for the gerbil DNLL, there is no linear dependence of best IPD on frequency found for the forebrain of the barn owl which would be consistent with the Jeffress model.

model may hold for the NL, but is not applicable to the forebrain.

To approximate the noise in the data, the conditional distribution $p_{r|\mu}$ was constructed by collecting rates r of all trials, independent of ITD and frequency that share the same mean rate μ. Then these data are fit by Gaussian distributions with variances that are shown in figure 4.3 C. The variability of the spike count across trials is found to be distinctly higher in the barn owl forebrain as compared to the situation in the gerbil DNLL (figure 4.3 C). In the barn owl forebrain, the variance $\mathrm{var}(s) = 1.05\,s$ of the spike count s is fairly Poissonian over the whole range of rates, whereas for the gerbil brainstem it is Poissonian only for small spike counts and sub-Poissonian for higher counts. This hints at coding schemes being different in the different nuclei of the two species. As pointed out in the previous chapter, for high noise, strong signal changes are preferred and thus peak-based codes are beneficial [72, 73]. In agreement with this prediction, peaks were found to be located more closely to the zero IPD for high noise levels. For lower noise levels, peaks were found mainly at ± 0.5 cyc (not shown).

Other than in the gerbil DNLL, activity in the barn owl forebrain is Poissonian, suggesting different coding schemes.

Since noise was found to be higher on average in the forebrain of the barn owl, the code was found to be more peak-based there as compared to the situation in the DNLL of the gerbil.

To further investigate the coding differences, the mutual information between ITD and rate is computed and compared to the results obtained from the DNLL of the gerbil.

4.2.1 Single-cell mutual information

To understand, how the observed activity codes the ITD, the mutual information between stimulus ITD τ and the corresponding firing rate r of a single cell,

$$I(r,\tau) = \sum_{r',\tau'} p_{r|\tau}(r'|\tau')\, p_\tau(\tau')\, \log_2\left(\frac{p_{r|\tau}(r'|\tau')}{p_r(r')}\right) \tag{4.1}$$

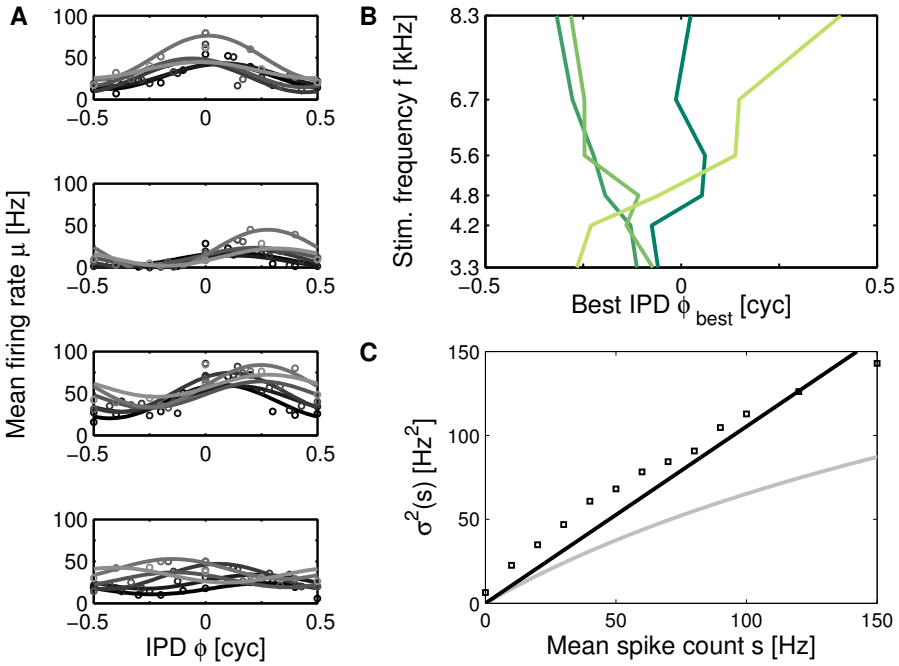

Figure 4.3: Frequency-variance of ITD sensitivity. (A) Tone delay functions for four exemplary forebrain neurons evoked by six stimulus frequencies (dark to light gray indicate low to high frequencies). Circles depict the means of measurements, the solid lines represent the corresponding fits (see Appendix). (B) Best IPD vs. stimulus frequency (phase-frequency curves) for the four neurons from A (dark to light green for upper to lower cells). Note, that a linear fit (defining CD and CP) is not possible for all cells here. (C) Variance σ^2 of the spike count distributions as a function of mean spike count s (squares averaged over all 113 neurons) and a linear (see Appendix) fit (black). For comparison, the variance (squares averaged over all 153 neurons) as obtained from the gerbil brainstem is also shown (gray).

is computed. The prior distribution p_τ of ITDs is obtained by assuming uniformly distributed dihedral angles (see Appendix). It depends on the maximum ITD $\tau_{\max}$ that confines the physiological range. The conditional distribution $p_{r|\tau}$ is given by the Gaussian distributions $p_{r|\mu}$ defined above wherein $\mu(\tau, f)$ is given by the fits to the tone delay functions (figure 4.3 C). The dependency on frequency is dismissed by summation, whereby frequencies are assumed to be distributed like $1/f$. The difference to a uniform distribution of frequencies is only minor (not shown).

Figure 4.4 B shows tone delay functions of the cell with the highest mutual information among the population of 28 cells. These curves vary over a huge range of rates. In contrast, figure 4.4 C shows tone delay functions of the cell with the lowest mutual information among the population. Compared to the best one, the activity of this cell is rather invariant to a change of ITD. Furthermore, the mean activity of this cell is much lower as compared to the best one. Figure 4.4 A illustrates the distribution of mutual information and compares it to the distribution as observed for gerbils (see previous chapter). The mutual information is distributed much more towards high values for the barn owl forebrain as compared to the gerbil DNLL (figure 4.4 A). In the previous chapter, the low mutual information suggested to take population codes into consideration. In what follows, population codes shall be considered for barn owls as well.

Single-cell mutual information between rate and ITD is distributed much more towards high values for owls compared to gerbils.

4.2.2 Population codes

Now the activity of forebrain neurons is analyzed as a whole, rather than for each cell separately. This is achieved by using simulated firing rate patterns of $N = 28$ neurons for different stimulus ITDs and frequencies (figure 4.5). In particular, rate patterns are used as input vectors to linear classifiers with output neurons, each of which

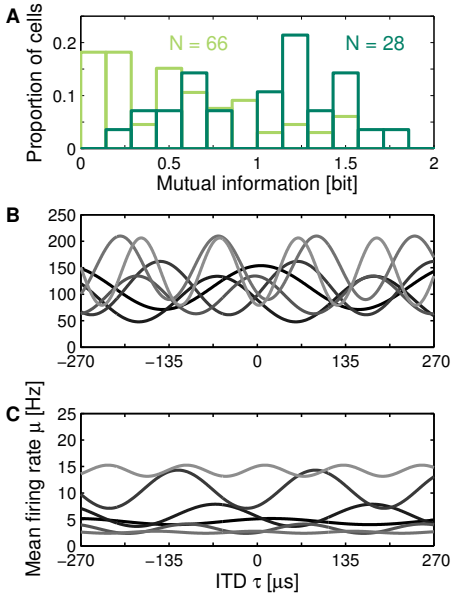

Figure 4.4: Mutual information between rate and ITD. (A) Distributions of mutual information of the 28 cells of the barn owl forebrain (dark green) and distribution of 66 cells of the gerbil (light green). The distribution of the barn owl is skewed towards high mutual information, whereas the distribution of the gerbil is skewed towards low mutual information. (B) Tone delay functions (fits) for the neuron with highest mutual information as evoked by six stimulus frequencies (dark to light gray indicate low to high frequencies). (C) Tone delay functions (fits) for the neuron with lowest information among the population. Compared to the one above, the response of this cell shows almost no variability against ITD. Additionally the mean response of this cell is much lower as compared to the one above.

encodes a different bin of azimuthal position (figure 4.5). Linear support vector machines [65, 66] are trained in a multiple fashion to classify the firing rate patterns into K categories representing azimuth bins of width $\delta\tau = 2\tau_{\max}/K$.

Classification errors of SVMs are much higher than psychophysically observed, which may be due to the low number of cells.

Figure 4.6 shows training and test errors as obtained for different numbers of bins K and training samples. The test error converges to an acuity of about 200 μs, which clearly disagrees with the psychophysical acuity of barn owls of only a few μs [84]. Restriction to fewer than six frequencies does not result in a significant error reduction. Reduction of the noise had little effect, too. Tuning of the regularization parameter and the precision parameter did not entail significant error reduction. Therefore it is assumed, that the number of $N = 28$ cells is not enough to reach classification errors consistent with psychophysical results (in the previous chapter, a number of $N = 66$ cells lead to reasonable errors).

Classification tasks suggest, that ITDs are encoded by neurons each of which is relevant to one specific azimuthal position (labeled line code).

Figure 4.7 shows the possibility of a population representation of ITDs by the activity of "grandmother neurons". K categories (labels) were defined, representing ITDs within bins of size $\delta\tau = 2\,\tau_{\max}/K$. Grandmother neurons are assumed to respond to ITDs from only few adjacent bins. A frequency-invariant representation of ITDs by the difference of the summed activities of both hemispheres was found to be inappropriate (not shown). As for gerbils, no correlation between single-cell mutual information and absolute weights of the classifier was found (not shown). This means, that few features of the population pattern may be enough to classify the ITD and that for each of the frequencies different features may be learned.

4.3 Discussion

Since the notion of information was mathematically formalized by Claude E. Shannon in 1949 [85], much of neuroscience was based

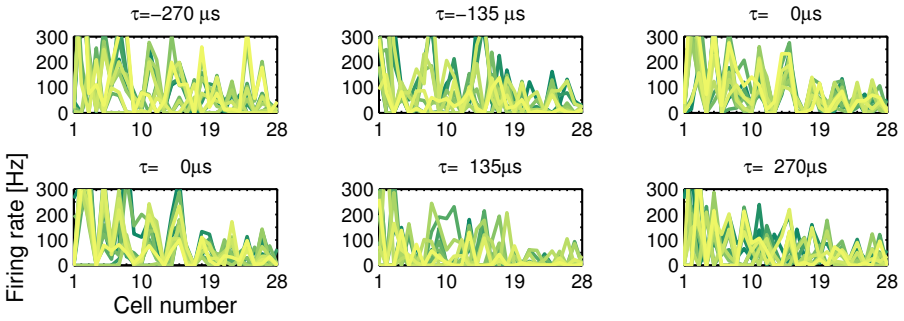

Figure 4.5: Realizations of the rate model. $N/2$ realizations as generated by the rate model of the population of $N = 28$ cells for five different ITDs. Stimulus ITDs are equally timed between $-\tau_{\max}$ and $\tau_{\max} = 270$ μs. The cells are sorted according to their average rate as resulting with sound coming from the leftmost direction, i.e. for an ITD of $\tau = -270$ μs. There is no systematic change of the population activity obvious as the sound source location changes from left to right. Due to the high noise, the rate response is very different even for equal stimulus conditions.

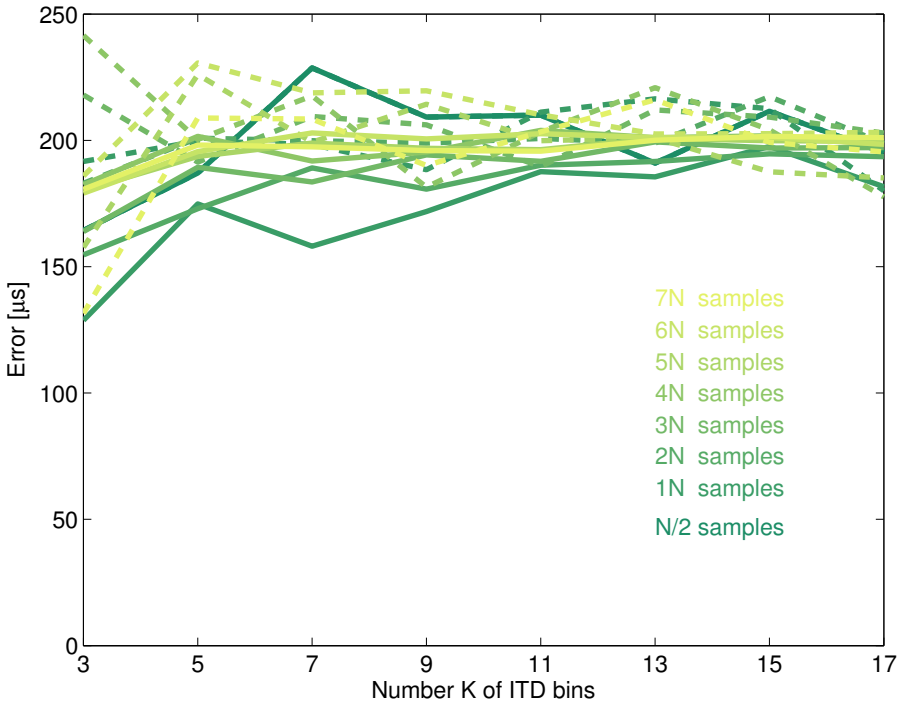

Figure 4.6: Training- and test errors. Test error of $N = 28$ units as a function of the number K of ITD bins for five different numbers of training samples ($N/2, 1\,N, 3\,N, 5\,N, 7\,N$ from dark to light green). Training errors are plotted as solid lines, test errors are plotted as dashed lines. Test errors decrease while training errors increase with the number of training samples, both saturating at a number of about $5\,N$.

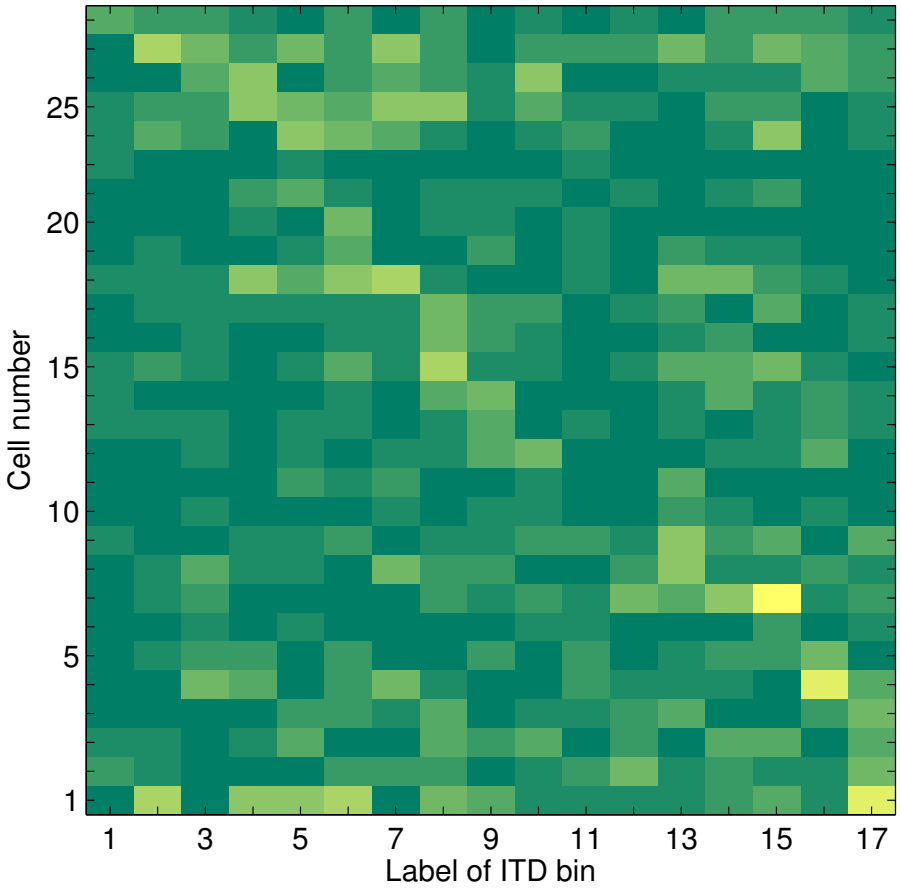

Figure 4.7: ABSOLUTE WEIGHTS. Absolute weights of the connections between input units (vertical axis) and output units (horizontal axis). The brighter the color, the higher the corresponding absolute weight. Support vector machines were trained with rates (obtained from the rate model) of the 28 cells, evoked by ITDs within the physiological range (subdivided in 17 ITD bins). The weights describe the state of learning after $5\,N$ training samples. Input units are sorted according to the labels of their maximum absolute weights. Most cells mainly respond to few adjacent bins, producing a labeled line code.

on information constraints [86, 87, 88, 89]. Invariance is evidently an important principle of information processing in the brain as well. Here, coding, constrained by both mutual information and invariance to frequency, was studied in case of the barn owl (and the gerbil).

The responses of neurons in the forebrain of barn owls change with both the ITD and the frequency of pure tone stimulus. As opposed to mammals, avian forebrain responses did not allow for the introduction of characteristic phases and characteristic delays as a means to study frequency invariance. Furthermore, the response noise was found much higher as compared to what was observed for gerbils. This provided evidence, that the two sets of data entail different ways of coding. As opposed to gerbils, a more peak-based code was found for barn owls.

The mutual information between stimulus ITD and response rate was computed. A frequency invariant representation was achieved by summing over the distribution of frequencies. Comparison to the mutual information as obtained for DNLL of gerbils revealed, that single cells of the barn owl's forebrain encode ITDs much more faithfully.

Adding noise, as constructed from the data, to tone delay functions provided the basis to study a frequency-invariant population representation of ITDs. The distribution of weights suggested a labeled line code as produced by grandmother neurons. Representations of ITDs by the difference of the summed activities of both hemispheres were found to be inappropriate. Errors, as made in the classification task, were found considerably higher for owls as compared to gerbils. This was leading to the assumption, that the number $N = 28$ of cells is too low to reach errors that agree with psychophysical experiments.

As for in the previous chapter, interpretation of the present data is complicated by the fact that the forebrain is not a primary nu-

cleus in which ITD responses are integrated. The response of forebrain neurons is already imposed by several processing steps. On the one hand, this makes forebrain data (if enough) well comparable to psychophysical experiments. On the other hand, the avian forebrain is further downstream as compared to the mammalian DNLL, which complicates the comparison of the two sets of data.

This chapter mainly showed, that ITDs are represented quite differently by the activity of the observed nuclei of the two species. Invariant representations of interaural time differences across species, however, are still insufficiently understood.

4.4 Outlook

For a better comparison to gerbil data, only *tone delay functions* were analyzed here. There are, however, *noise delay functions* from the same animals available as well [4]. There was a high correlation found between noise delay functions and the sum of tone delay functions [4]. Therefore Fourier decompositions of noise delay functions provide a higher number of tone delay functions, which improves statistics particularly in classification tasks.

4.5 Appendix

4.5.1 Stimuli

White noise bursts ($0.1 - 20$ kHz) were used and tone beeps of 100 ms length with 5 ms cosine start and end ramps for dichotic stimulation. Signals were sampled at 50 kHz, digital-to-analog converted, attenuated, anti-alias filtered, power amplified and presented through calibrated earphones. To detect neural activity, noise bursts of varying ITD were played while slowly advancing the electrode. For each neuron first the ITD range between ± 270 μs

in steps of 30 μs was sampled using an interaural level difference (ILD) of zero dB. Via online analysis, a first estimate of the noise-delay curve was obtained. Then the neurons interaural level difference was assessed, tuning in a similar way between $\pm$20 dB in steps of 1 dB, while holding the ITD constant at the value that the neuron responded maximally to. If the neurons best ILD was different from zero, the noise delay curve was recorded again, holding the ILD at the neurons preferred value. The neurons frequency tuning was assessed by playing tones of frequencies between $500 - 9500$ Hz in steps of 500Hz, while keeping the ITD and ILD constant the neurons preferred values. This curve is referred to as iso-ITD frequency tuning or briefly frequency tuning curve in the following. Stimuli were always presented a minimum of five times in block-wise random order. Inter-trial interval was 1 s. Tone-delay curves were obtained in an analogous way to the noise-delay curves. Tone beeps were interaurally delayed using ITDs that regularly sampled one stimulus period. Typical stimulation frequencies had periods that were integer multiple of 30 μs: 2381, 2564, 3030, 3333, 3704, 4167, 4762, 5555, 6666 or 8333 Hz. For very high ($>$ 6667 Hz) or very low frequencies ($<$ 2381 Hz) a more adequate ITD sampling step was chosen. The sampled ITD range for tones included a minimum of one period of the stimulation frequency.

4.5.2 Tone delay functions

Like for gerbils, the tone delay functions are considered to depend on the interaural phase difference (IPD) $\phi := f \times \text{ITD}$ solely. The rates were averaged over all repetitions of the respective pure tone stimulus and approximated by

$$\mu_f(\phi) = 2\, r_f \cos\left(\phi + \phi_{\text{best}\,f}\right) + M_f\,, \tag{4.2}$$

i.e. the first component of their Fourier series. The parameters r_f, $\phi_{\text{best}\,f}$ and M_f are obtained as follows

$$z_f = N^{-1} \sum_{\phi} r_f(\phi) \exp(-2\pi\, i\, \phi) \,. \tag{4.3}$$

The rate is obtained by $r_f(\phi) = \text{abs}(z_f) + M_f$ where M_f is the rate averaged over IPDs. The best IPD is given by $\phi_{\text{best}\,f} = \arg(z_f)$.

4.5.3 Rate distributions

As in subsection 3.5.5, an estimate for the conditional probability distribution $p_{r|\mu}$ is required. This is the probability of observing a firing rate r given a stimulus that evoked mean response rate μ. Like for gerbils, a Gaussian, as given by equation (3.6), is fit to the rate distributions. Unlike for gerbils, the variance $\text{var}(r)$, as obtained from the spike count (pooled over all cells), is not fit logarithmically, but linearly by

$$\text{var}(r) = 1.05\,\text{Hz} \times r \,.$$

Thus, the distribution $p_{r|\mu}$ is fairly Poissonian over the whole range of the mean response rate.

4.5.4 Linear classifiers

As for gerbils, the machine learning package Shogun [66] has been used to study the representation of population responses to ITDs by grandmother neurons. Here, however, training was not done in a one-vs.-one mode, but multiple-wise (compare to previous chapter for details).

Chapter 5

A method to estimate network connectivity

5.1 Introduction

In the previous two chapters data are analyzed that were obtained by recording from only one neuron at a time. Population codes hereby refereed to a pseudo population, since neuronal activity was recorded successively from several animals. This approach is based on the assumption, that the single experiments are decently reproducible with respect to spike counts. There are codes that are based on the exact relative timing of spikes of a neuronal population. Spike sequences are generally less reproducible than spike counts. Thus parallel recordings are sometimes preferable over sequential ones. Multi-electrode arrays serve to simultaneously record from many neurons. The propagation of parallel recording techniques led to a realignment of the analysis from single-spike statistics [90, 91] to the analysis of neural population activities [92, 93, 94, 89, 95]. The stimulus encoded by the activity of a population of source neurons is read out by target neurons at some point. The connection between two neurons hereby quantifies, how the spiking of one neuron enhances or reduces the spiking of a second one. Consequently, the question was raised, whether it was possible to infer the underlying connectivity from parallel recordings. Multi-transistor arrays

The connection between two neurons influences the effect spiking of the first neuron has on spiking of the second one.

One strives for a method to estimate the *connectivity* from parallel recordings.

today typically record from several hundreds up to thousands of neurons [96], hence, the number of potentially connected pairs add up to tens of thousands. Therefore, in spite of the computational power available today, methods should be computationally efficient. Some of the more recent approaches shall be reviewed below.

Methods should be both exact and efficient.

Makarov et al. [97] create a deterministic network model, whose dynamic behavior fits experimental data. It includes a set of coupled differential equations that depend on parameters that are unknown beforehand. Then, the parameters, among them the $N \times N$ matrix of connection strengths, are determined by minimizing the difference between the model- and the experimental interspike interval statistics. Experimental spike times are generated by a leaky integrate-and-fire (LIF) network. Besides estimates of connection strengths, they also obtain the time constants involved. However, the method assumes the activity to be sustained by constant currents. Furthermore the computational requirements, seem somewhat prohibitive, as the largest network studied, consists of $N = 5$ units.

Yu et al. [98], assuming all parameters are known beforehand, vary the connectivity matrix of a model network until it synchronizes with the experimental network. The method has been shown to be efficient up to size $N = 17$ for chaotic Lorenz oscillators. In a further step, Yu and Parlitz [99] improved the above method of synchronization by including external neurons that drive the network towards steady states, at which they are able to better reconstruct the connectivity.

Timme et al. [100] look at collective response to systematically changing input, to reduce the amount of possible connections consistent with the observed response. As explicitly computed for sparsely connected phase-locked oscillators only, for each of the inputs, a linear system of N equations has to be solved. Unlike the above methods, this one works without exact knowledge of the

underlying network parameters reasonably for $N \sim 100$ units.

In what follows, a new method for estimating the effective network connectivity is introduced. Unlike a *structural* connection that only requires two neurons to be physically connected, an *effective* connection additionally requires, that one of the neurons exerts measurable influence over the other [101].

The new method utilizes the correlation of coupling strength and mutual information between the spike times of a target neuron and a variable similar to its membrane potential, as it would be caused by a potential source neuron.

5.2 Theory

If a pair of neurons is connected via a synapse, there is potentially a change in the target neuron's membrane potential, caused by the source neuron. When mathematically modeling the membrane potential, it may be called *virtual*, since beforehand one doesn't know, if two neurons are connected. The virtual potential (VP) is defined as

The VIRTUAL POTENTIAL (VP) is defined as the membrane potential of a target neuron as affected by some potential source neuron.

$$v_i(t) := \sum_{t_i} \exp\left[-\left(t - t_i - t_{\text{delay}}\right)/\tau\right] . \tag{5.1}$$

The VP is thought to resemble the membrane potential of the target neuron at time $t \in [t_0, T]$, as solely caused by the source neuron i spiking at past times $t_i \in \left[t_0, t - t_{\text{delay}}\right]$, delayed by some synaptic transmission time t_{delay} (figure 5.1).

As time t is subdivided into intervals of length Δt, v_i becomes a vector of length $B = \lfloor T/\Delta t \rfloor$. The spike sequence of a source neuron is represented by a vector $\boldsymbol{\sigma}_j \in \{0,1\}^B$ of the same length in order to compute the mutual information for all possible pairs of

The mutual information (MI) between spiking of target neurons and the VP of potential source neurons is computed for all pairs.

source neuron i and target neuron j given by

$$I\left(v_i;\sigma_j\right)=\sum_{\{\sigma_j\}}p_\sigma\left(\sigma_j\right)\sum_{\{v_i\}}p_{v|\sigma}\left(v_i|\sigma_j\right)\,\log_2\frac{p_{v|\sigma}\left(v_i|\sigma_j\right)}{p_v\left(v_i\right)}\ . \tag{5.2}$$

Usually, there is a reset of the membrane potential of the target neuron to its resting value after every time it spikes. By introducing a target-dependent reset into the source-dependent variable VP, however, one inevitably creates mutual information regardless of whether two neurons are connected or not. If a pair is connected, a spike of the target neuron leads to a reset of its membrane potential. Thus the VP as generated by the source neuron should resemble that reset as well. However, since most pairs of neurons are unconnected, this reset is generally left out.

The MI is then related to the connection strength between target and source neuron.

In a nutshell, the method relates $I\left(v_i;\sigma_j\right)$ to the corresponding connection strength w_{ij}.

5.3 Results

The method is examined on data generated by an implementation of a LIF network, available as the Python module *Brian* [102]. The activity of a target neuron is determined by the system of differential equations

$$\tau\,\frac{\mathrm{d}u\left(t\right)}{\mathrm{d}t}=-u\left(t\right)+u_{\mathrm{rest}}+R\,I_{\mathrm{src}}\left(t\right) \tag{5.3}$$

$$\tau_{\mathrm{src}}\,\frac{\mathrm{d}I_{\mathrm{src}}\left(t\right)}{\mathrm{d}t}=-I_{\mathrm{src}}\left(t\right)+I_{\mathrm{ext}}\left(t\right) \tag{5.4}$$

where u is the membrane potential, I_{src} the sources' input current, I_{ext} is some sustaining external current, τ and τ_{src} is the time constants with which the membrane potential and the sources' input currents decay. At the time u reaches the threshold potential u_{thr},

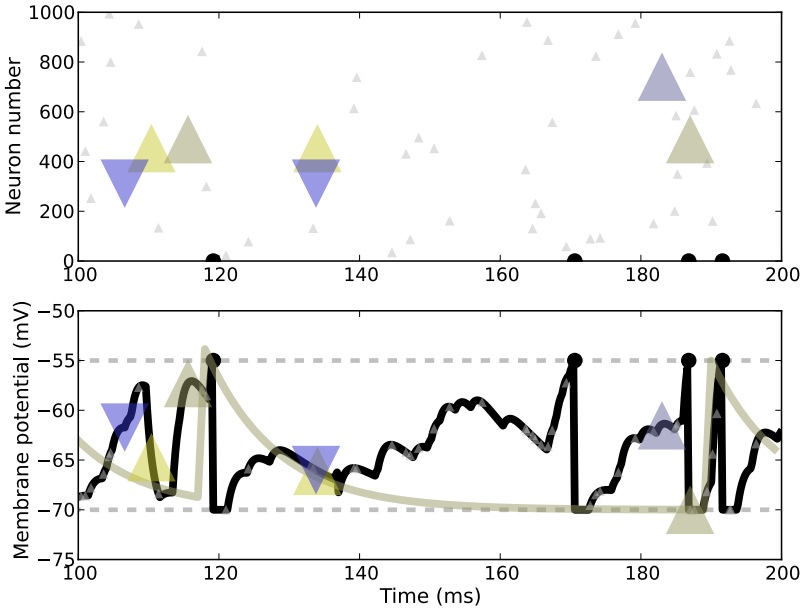

Figure 5.1: Upper panel: Simulated spike raster. Spike time vs. neuron number of all source neurons connected to target neuron 0. Upward pointing triangles represent excitatory, downward pointing ones inhibitory input. The marker size corresponds to the weight of the connection. External driving neurons are depicted in light gray, internal neurons in different colors. The black semicircles depict resulting spikes of the target neuron. Lower panel: Resulting membrane potential and virtual potential. Time course of the membrane potential of the target neuron is printed in black. Plotted on top are the sources spikes at the moments they occur (their effect is delayed by 2 ms). The VP as caused by one of the sources, as well as the corresponding spikes, are shown in olive. The VP is high at spike times of the target neuron that are mainly due to that very source.

the neuron spikes and its membrane potential is reset to the resting value u_{rest}, where it remains for the refractory period t_{ref}. The current is usually contributed by several source neurons and weighted by their particular synaptic strengths w.

VP (see definition 5.1) is known to solve equations (5.3), if the external current behaves like a pulse, i.e. for $\tau_{\text{src}} \to 0$ [103].

Figure 5.2 represents a typical network and the activity of its LIF neurons. Based on activity patterns like this, the connectivity shall be estimated.

The mutual information (5.2) between the VP of potential sources and the spike sequence of targets is computed for all pairs of neurons in a network (figure 5.3). There were huge differences in mutual information across target neurons found. When the mutual information of all pairs of targets and sources was gathered in a single histogram, the mutual information of unconnected pairs in some cases exceeded that of connected pairs. In what follows, histograms thus always refer to a single target and all of its potential sources.

The method is evaluated with a simulated network with connection strengths being of the same magnitude but different polarity.

First LIF network are considered in which weights assume one of three possible values, $-w$, 0 and w.

When confronted with experimental data, the method yields distributions of mutual information for pairs of neurons (figure 5.3). One then has to decide for a threshold z, assuming only pairs above that threshold as connected (figure 5.3, lower panel). This approach leads to a false positive rate (FPR) α and a true positive rate (TPR) β. The TPR is the frequency with which a *connected* pair of neurons is found above threshold. The FPR is the frequency with which an *unconnected* pair of neurons is found above threshold. By varying the threshold, α and β trace out a curve, referred to as the receiver operating characteristic curve (ROC curve). For any threshold, one prefers α to be large as compared to β. Therefore, the area $A\prime \in [0, 1]$ below the ROC curve is chosen as a measure

Definition of a threshold of MI leads to a FALSE POSITIVE - (FPR) and a TRUE POSITIVE RATE (TPR) when classifying all pairs above threshold as connected.

The area under the curve of FPR against TPR, parametrized with the threshold, is used as an evaluation measure of the method.

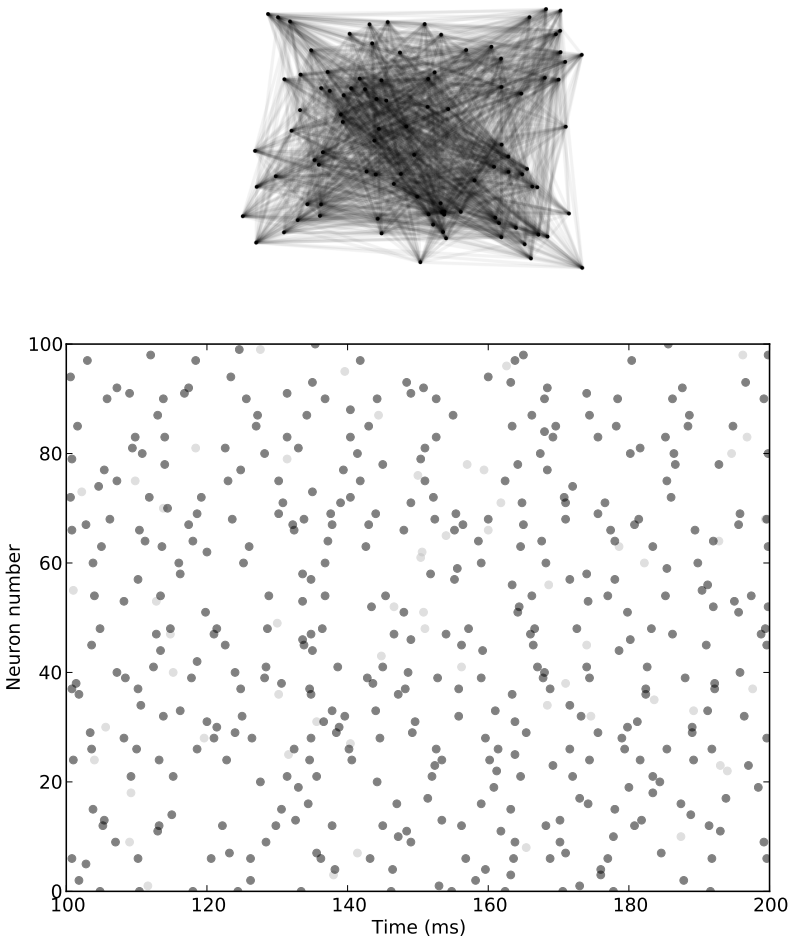

Figure 5.2: Upper panel: Network graph. Subnetwork of 100 neurons of a network of 1000 with an average of 233 sources connected to each neuron. Lower panel: Spike raster. Spike time vs. neuron number of the above network within a 100 ms period. External sustaining spikes are depicted in light gray, internal neurons in dark gray. Based on similar spike rasters and certain knowledge about the biophysics involved, the challenge is to find a method, capable of revealing as reliably as possible the underlying connectivity.

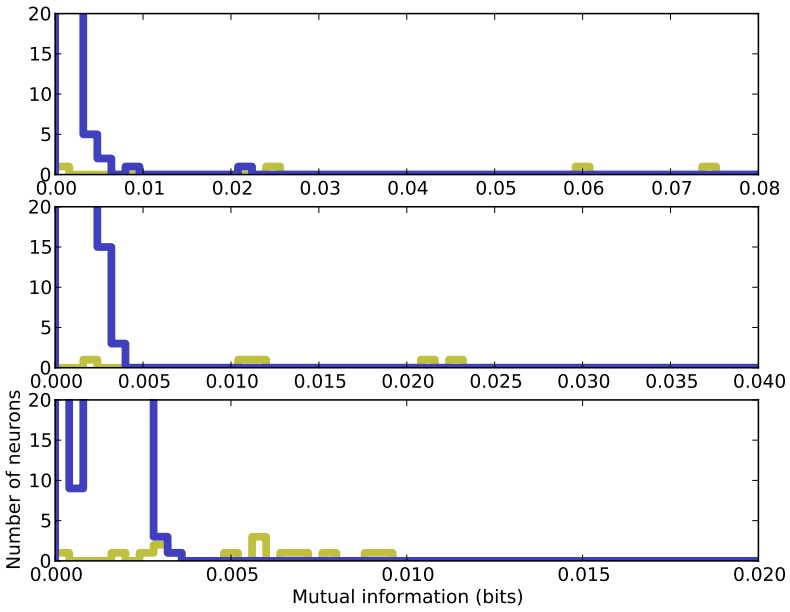

Figure 5.3: HISTOGRAMS OF MUTUAL INFORMATION. Histograms of mutual information between the VP and and the spike sequence for connected (yellow) and unconnected (blue) pairs of neurons. In the upper plot the target neuron receives input from four sources, in the middle plot from five and in the lower plot from fifteen sources. The histograms in each of the three plots refer to mutual information between spiking of only one target neuron and the VP of all other neurons. Mind, that the scales of the horizontal axes are different.

to evaluate the method (figure 5.4). The closer the area is to one, the better the method works for a certain set of spike sequences. An area of one would mean no intersection of the distributions of connected and unconnected neuron pairs and thus a false negative rate of zero for a properly chosen threshold. A straight line from $\alpha = \beta = 1$ to $\alpha = \beta = 0$, with an area of $A\prime = 1/2$ under it, represents the case where the distributions of mutual information of connected and unconnected pairs are indistinguishable.

ROC curves have two obvious drawbacks. At first, they are only suited for analyzing binary data, i.e. data that are either positive (connected) or negative (unconnected). Here, however, only binary data are analyzed. Secondly, when the network is very sparse, there are considerably more unconnected pairs of neurons than connected ones. Despite a low FPR and a high TPR, the true positive pairs might *get lost* in the large amount of false negative pairs. Therefore ROC curves should not be the only means of evaluation and distributions of mutual information as such should be taken into account, too (not shown except in figure 5.3).

How well a connection can be detected by the method seems to depend on the amount of sources a target neuron is connected to (figure 5.3). Therefore, the method is applied to data that were generated by systematically changing the amount of sources per neuron, whilst keeping the average firing rate of the whole population constant. To evaluate the method in the different instances, the dependence of $A\prime$ on the average amount of sources per neuron s is computed (figures 5.5). Figure 5.6 depicts the dependence of the area under curve on the average amount of sources. The more sources are connected, the worse the method works. Each of the networks consists of $N = 1000$ neurons. On average, each network is firing at an average rate of ~ 40 Hz, which leads to an average of 1000 spikes per neuron in the 25 seconds of the simulation. External neurons, that are not part of the analyses, sustain the network

The method is evaluated for different numbers of SOURCES PER NEURON, i.e. the numbers of neurons a target neuron is connected to.

The higher the number of sources per neuron, the worse the method works (under the circumstances).

activity (see Appendix). Rates are approximately kept constant by lowering the weights, while the number of sources per neuron is increased. The connections, sustaining neurons make, are unaltered. This approach reduces the effect internal connections have, as compared to connections from outside. For this reason, the method works better for a smaller amount of sources per neuron.

5.4 Discussion

Extracting connectivity of a neuronal network, of which only the spike times are known, is a problem that much attention has been drawn to recently [97, 100, 98, 99, 104].

The present chapter describes a novel method to estimate network connectivity. Many methods, two of which were briefly reviewed above [98, 99], assume parameters to be given. This method works without exact knowledge of the underlying network parameters. Simulations (not presented here) showed, that neither time constants nor delays nor the exact shape of the VP (replaced by an alpha function), are of significance.

To the authors knowledge, all comparable methods developed so far require some kind of minimization procedure. Minimization, however, is time consuming. With an increasing number of neurons considered, efficiency becomes a crucial quality. The method developed here is based on the computation of a simple information measure and may thus be the most efficient one to date. This makes it a useful tool to study data sets of realistic sizes. All methods known to the author, including the briefly reviewed ones above [97, 98, 99, 100], can deal with networks of no more than $N \sim 100$ neurons. Application of the new method to $N = 1000$ spike sequences of 25 s duration, with time bins of 1 ms, took about 1 h of processing time on a 1 GHz core. Parallel execution on 20 cores thus means processing of more than $N = 4000$ neurons in the

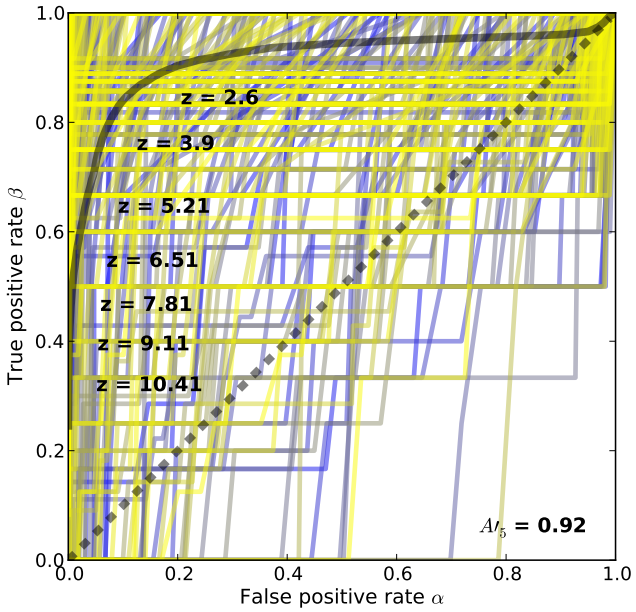

Figure 5.4: Receiver operating characteristic curves. ROC curves for all target neurons separately are depicted in color. Each point on a curve correspond to a different threshold z. As the threshold is varied, these points trace out the ROC curves. The black curve is the average ROC curve of the network with an average of five sources per neuron. The average threshold values are given in units of 10^{-3} bits. There is an average area of $A\prime_5 = 0.92$ under all curves and thus under the average curve as well. The dashed straight line runs from $\alpha = \beta = 1$ to $\alpha = \beta = 0$ representing equality of the two distributions.

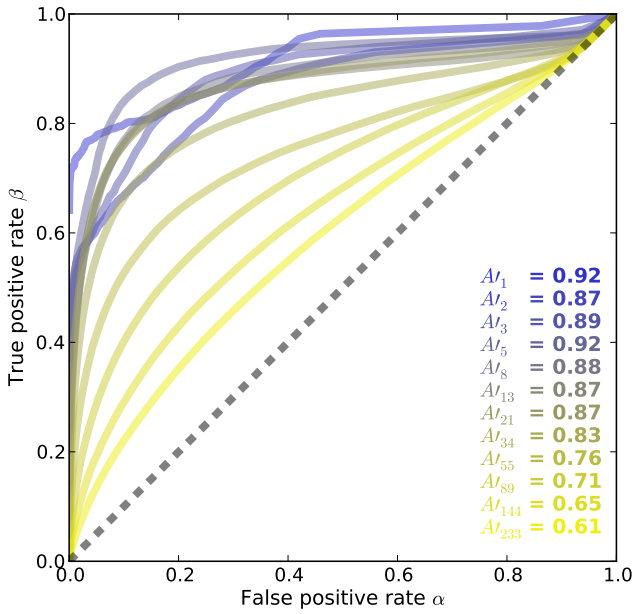

Figure 5.5: AVERAGE ROC CURVES. Average ROC curves, as computed for networks with an increasing number of sources per neuron, are shown in colors from blue to yellow. The corresponding areas under the curves are colored the same way.

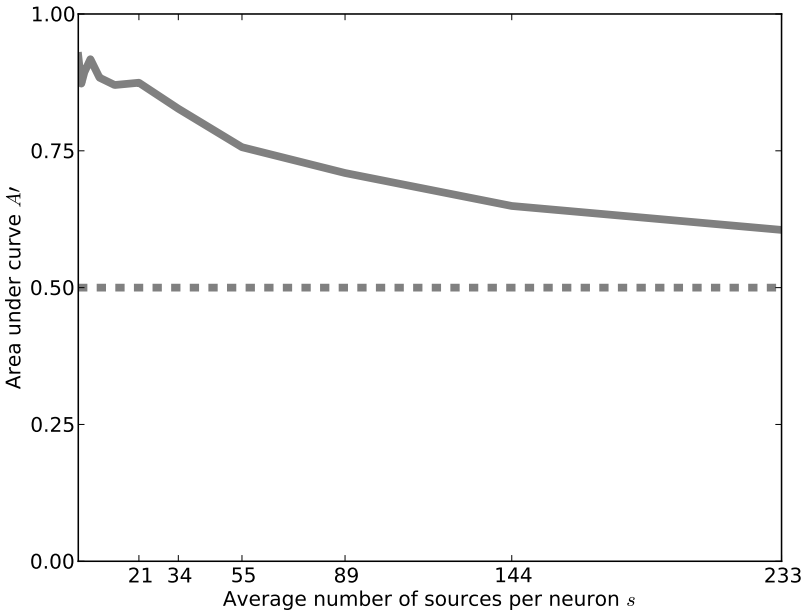

Figure 5.6: EVALUATION. Area under the average ROC curves as computed for networks with an varying number sources per neuron $s \in \{1, 2, 3, 5, 8, 13, 21, 34, 55, 89, 144, 233\}$. The fewer sources a target neuron receives input from, the better the method works.

same amount of time.

Regarding its efficiency and the fact that parameters need not to be known, the presented method improves on existing ones.

5.5 Outlook

The evaluation was carried out here for different time constants, delays, VPs, and, most extensively, numbers of connections. In a continuation of this work, an equivalent evaluation needs to be carried out for the other parameters (see table 5.2) involved. Once this is done, the method should be evaluated further with different regimes of network dynamics to finally be applied to real data. Parallel recordings done in vivo serve a rather incomplete picture of the real situation. Due to the distribution of the multiple electrodes of an electrode array, much of the activity of interest is not recorded. Dissociated neuronal cultures, however, can provide quite complete data. Spike sequences, for example, may be inferred from calcium imaging of neuronal cultures by sequential Monte Caro methods [105]. The present method may then also be compared to an earlier attempt that does not require any spike sequence inference [106].

5.6 Appendix

5.6.1 Network parameters

Each neuron was initialized with a membrane potential $u_{\text{init}} = V_{\text{reset}} + r\,(V_\Theta - V_{\text{reset}})$ where $r \in [0, 1]$ is a different random number for every neuron.

All neurons of the external network spike in random order every 200 ms, leading to an excitatory input rate of 500 Hz to every neuron of the internal network.

Quantity	Value	Meaning
N	1000	Number of intern neurons
N_{ext}	1000	Number of external neurons
V_{reset}	-70 mV	Reset potential
V_{rest}	-70 mV	Resting potential
V_{Θ}	-55 mV	Threshold potential
τ	10 ms	Time constant of membrane potential
τ_{src}	1 ms	Source current time constant
t_{ref}	2 ms	Refractory period
t_{delay}	3 ms	Axonal delay time
T	25 s	Simulation time
c_{ext}	100	Number of external sources
w_{ext}	25 mV	Weight of external inputs

Table 5.1: NETWORK PARAMETERS USED FOR SIMULATIONS. The parameters were left unchanged in all simulations. The choice of parameters that were changed for evaluating the method are listed in table 5.2.

No. of sources s	Weights w
1	1400 mV
2	172.5 mV
3	122.5 mV
5	82.5 mV
8	70 mV
13	53 mV
21	40 mV
34	31 mV
55	25 mV
89	19 mV
144	15.5 mV
233	12.75 mV

Table 5.2: Network parameters used for simulations. An average of half of the connections of the internal network are excitatory, the other half inhibitory.

Chapter 6

Epilog

Mammals and birds evolved equivalent concepts of sound detection. In both species, frequencies are mapped to different places of the basilar membrane due to variable mechanical properties. Deflections of hair cells, that distribute along the cochlear partition, provide transduction of mechanical into electrical signals. There are, however, differences between the two concepts. For example, the avian cochlea displays a the shape of a bent tube, while mammalian cochleae look invariably coiled. Moreover, mechanical feedback amplifications provided by outer hair cells are found solely in mammals. Despite the aforementioned differences, the model of sound decomposition, as introduced in this thesis, is capable of describing and interpreting both systems. It is optional to involve amplification by outer hair cells and there is no dependence on the curvature of the cochlear duct. It is just a matter of the choice of parameters that makes the model hold for different species.

As previously mentioned, mammals and birds have evolved profoundly different concepts of how to localize sound by making use of interaural time differences. Yet, this thesis contains a single approach to better understand coding strategies as determined by the underlying neuronal circuitry. Information theory is used to evaluate frequency-invariant coding of interaural time differences by the activity of single cells, and tools of machine learning are employed to study codes as exhibited by populations of neurons.

Data obtained from the gerbil and the barn owl are shown to entail different coding strategies. The way in which invariance is included may serve as an example for future investigations.

Neural pathways, like the auditory pathways described throughout this thesis, are genetically predefined. They are fundamentally alike for all animals assigned to the same species. The connections single neurons make to each other, however, are highly variable. This variability is refered to as *learning*. What animals learn throughout their lives is usually quite different and hence connectivity is distinct in every animal. The method of connectivity inference, that was introduced in this thesis, is applicable to all subjects under study. This method may serve as an universal starting point to infer neuronal circuitry based on multi-neuron behavior, and its availability is therefore paramount as more and more experimentalists strive to simultaneously record population activity. However, the work is yet complete.

In summary it can be said, therefore, that this thesis contains interesting insights as well as concepts that are worth being continued.

Bibliography

[1] H. Lüling, J.-M. P. Franosch, and J. L. van Hemmen. A two-dimensional cochlear fluid model based on conformal mapping. *Journal of the Acoustical Society of America*, 128(6):3577–3584, 2010.

[2] I. Siveke, M. Pecka, A. H. Seidl, S. Baudoux, and B. Grothe. Binaural response properties of low-frequency neurons in the gerbil dorsal nucleus of the lateral lemniscus. *Journal of Neurophysiology*, 96(3):1425–1440, 2006.

[3] H. Lüling, I. Siveke, B. Grothe, and C. Leibold. Frequency-invariant representation of interaural time differences in mammals. *PLoS Computational Biology*, 7(3):11, 2011.

[4] K. Vonderschen and H. Wagner. Auditory forebrain neurons construct characteristic phase delays from a time delay map (in preparation).

[5] H. Gray and H. V. Cater. *Anatomy, descriptive and surgical.* Churchill Livingstone, London, 1858.

[6] J. B. Allen. Two-dimensional cochlear fluid model: new results. *Journal of the Acoustical Society of America*, 61(1):110–119, 1977.

[7] M. B. Lesser and D. A. Berkley. Fluid mechanics of the cochlea. Part 1. *Journal of Fluid Mechanics*, 51:497–512, 1972.

[8] J. Lighthill. Energy flow in the cochlea. *Journal of Fluid Mechanics*, 106:149–213, 1981.

[9] F. Mammano and R. Nobili. Biophysics of the cochlea: linear approximation. *Journal of the Acoustical Society of America*, 93(6):3320–3332, 1993.

[10] O. F. Ranke. Theory of operation of the cochlea: a contribution to the hydrodynamics of the cochlea. *Journal of the Acoustical Society of America*, 22(6):772–777, 1950.

[11] M. R. Schroeder. An integrable model for the basilar membrane. *Journal of the Acoustical Society of America*, 53(2):429–434, 1973.

[12] W. M. Siebert. Ranke revisited - a simple short-wave cochlear model. *Journal of the Acoustical Society of America*, 56(2):594–600, 1974.

[13] N. Sieroka, H. G. Dosch, and A. Rupp. Semirealistic models of the cochlea. *Journal of the Acoustical Society of America*, 120(1):297–304, 2006.

[14] C. R. Steele and L. A. Taber. Comparison of WKB and finite difference calculations for a two-dimensional cochlear model. *Journal of the Acoustical Society of America*, 65(4):1001–1006, 1979.

[15] E. G. Wever. Development of traveling-wave theories. *Journal of the Acoustical Society of America*, 9B:1319–1324, 1962.

[16] M. A. Viergever. *Mechanics of the Inner Ear.* Delft University Press, Delft, 1980.

[17] C. R. Steele. Behavior of the basilar membrane with pure-tone excitation. *Journal of the Acoustical Society of America*, 55(1):148–162, 1974.

[18] C. R. Steele and L. A. Taber. Three-dimensional model calculations for guinea pig cochlea. *Journal of the Acoustical Society of America*, 69(4):1107–1111, 1981.

[19] M. H. Holmes. An analysis of a low-frequency model of the cochlea. *Journal of the Acoustical Society of America*, 68(2):482–488, 1980.

[20] E. de Boer. The "inverse problem" solved for a three-dimensional model of the cochlea. I. Analysis. *Journal of the Acoustical Society of America*, 98(2):896–903, 1995.

[21] E. De Boer, A. L. Nuttall, and C. A. Shera. Wave propagation patterns in a "classical" three-dimensional model of the cochlea. *Journal of the Acoustical Society of America*, 121:352–362, 2007.

[22] H. L. Hawkins, T. A. McMullen, A. N. Popper, and R. R. Fay. *Auditory Computation.* Springer, New York, 1996.

[23] R. Nobili and F. Mammano. Biophysics of the cochlea. II: stationary nonlinear phenomenology. *Journal of the Acoustical Society of America*, 99(4 Pt. 1):2244–2255, 1996.

[24] H. Lamb. *Hydrodynamics.* Cambridge University Press, Cambridge, 1932.

[25] M. A. Viergever and J. J. Kalker. On the adequacy of the Peterson-Bogert model and on the effects of viscosity in cochlear dynamics. *Journal of Engineering Mathematics*, 8(2):149–156, 1974.

[26] M. A. Viergever and J. J. Kalker. Localization of non-linearities in the cochlea. *Journal of Engineering Mathematics*, pages 11–20, 1975.

[27] R. V. Churchill and J. W. Brown. *Complex Variables and Applications*. McGraw-Hill, Columbus, 1990.

[28] E. C. Titchmarsh. *The Theory of Functions.* Oxford University Press, Oxford, 1939.

[29] L. Robles and M. A. Ruggero. Mechanics of the mammalian cochlea. *Physiological Reviews*, 81(3):1305–1352, 2001.

[30] P. Dallos, A. N. Popper, and R. R. Fay. *The Cochlea.* Springer Handbook of Auditory Research. Springer, New York, 1996.

[31] W. Hemmert, U. Düring, M. Despont, U. Drechsler, G. Genolet, P. Vettinger, and D. M. Freeman. *A life-sized, hydrodynamical, micromechanical inner ear.* World Scientific, Singapore, 2003.

[32] R. Nobili, F. Mammano, and J. Ashmore. How well do we understand the cochlea? *Trends in Neurosciences*, 21(4):159–167, 1998.

[33] P. Mistrík, C. Mullaley, F. Mammano, and J. Ashmore. Three-dimensional current flow in a large-scale model of the cochlea and the mechanism of amplification of sound. *Journal of the Royal Society Interface*, 6(32):279–291, 2009.

[34] W. H. Press, S. A. Teukolsky, and B. P. Flannery. *Numerical Recipes in C*. Cambridge University Press, Cambridge, 1992.

[35] C. H. Brown, T. Schessler, D. Moody, and W. Stebbins. Vertical and horizontal sound localization in primates. *Journal of the Acoustical Society of America*, 72(6):1804–1811, 1982.

[36] T. C. T. Yin. Binaural interaction in low-frequency neurons in inferior colliculus of the cat. I. Effects of long interaural delays, intensity, and repetition rate on interaural delay function. *Journal of Neurophysiology*, 50(4):981–999, 1983.

[37] T. C. T. Yin and J. C. Chan. Interaural time sensitivity in medial superior olive of cat. *Journal of Neurophysiology*, 64(2):465–488, 1990.

[38] C. E. Carr and M. Konishi. A circuit for detection of interaural time differences in the brain stem of the barn owl. *The Journal of Neuroscience*, 10(10):3227–3246, 1990.

[39] D. McAlpine, D. Jiang, and A. R. Palmer. A neural code for low-frequency sound localization in mammals. *Nature Neuroscience*, 4(4):396–401, 2001.

[40] D. C. Fitzpatrick and S. Kuwada. Tuning to interaural time differences across frequency. *The Journal of Neuroscience*, 21(13):4844–4851, 2001.

[41] A. Brand, O. Behrend, T. Marquardt, D. McAlpine, and B. Grothe. Precise inhibition is essential for microsecond interaural time difference coding. *Nature*, 417(5):543–547, 2002.

[42] C. Köppl and C. E. Carr. Maps of interaural time difference in the chicken's brainstem nucleus laminaris. *Biological Cybernetics*, 98(6):541–559, 2008.

[43] C. E. Carr, D. Soares, J. Smolders, and J. Z. Simon. Detection of interaural time differences in the alligator. *The Journal of Neuroscience*, 29(25):7978–7990, 2009.

[44] J. W. S. Rayleigh. On our perception of sound direction. *Philosophical Magazine*, 13(73-78), 1907.

[45] F. L. Wightman and D. J. Kistler. The dominant role of low-frequency interaural time differences in sound localization. *Journal of the Acoustical Society of America*, 91(3):1648–1661, 1992.

[46] J. Blauert. *Spatial hearing: the psychophysics of human sound localization.* MIT Press, Boston, 1997.

[47] D. J. Tollin and T. C. T. Yin. Interaural phase and level difference sensitivity in low-frequency neurons in the lateral superior olive. *The Journal of Neuroscience*, 25(46):10648–10657, 2005.

[48] C. E. Carr, D. Soares, S. Parameshwaran, and T. Perney. Evolution and development of time coding systems. *Current Opinion in Neurobiology*, 11(6):727–733, 2001.

[49] B. Grothe. New roles for synaptic inhibition in sound localization. *Nature Reviews. Neuroscience*, 4(7):540–550, 2003.

[50] C. Köppl. Evolution of sound localisation in land vertebrates. *Current Biology*, 19(15):635–639, 2009.

[51] D. McAlpine. Sound localization and delay lines do mammals fit the model? *Trends in Neurosciences*, 26(7):347–350, 2003.

[52] N. S. Harper and D. McAlpine. Optimal neural population coding of an auditory spatial cue. *Nature*, 430(8):682–686, 2004.

[53] T. M. Shackleton, B. C. Skottun, R. H. Arnott, and A. R. Palmer. Interaural time difference discrimination thresholds for single neurons in the inferior colliculus of Guinea pigs. *The Journal of Neuroscience*, 23(2):716–724, 2003.

[54] B. C. Skottun, T. M. Shackleton, R. H. Arnott, and A. R. Palmer. The ability of inferior colliculus neurons to signal differences in interaural delay. *Proceedings of the National Academy of Sciences of the United States of America*, 98(24):14050–14054, 2001.

[55] M. Pecka, I. Siveke, B. Grothe, and N. A. Lesica. Enhancement of ITD coding within the initial stages of the auditory pathway. *Journal of Neurophysiology*, 103(1):38–46, 2010.

[56] A. R. Palmer, L.-F. Liu, and T. M. Shackleton. Changes in interaural time sensitivity with interaural level differences in the inferior colliculus. *Hearing Research*, 223(1-2):105–113, 2007.

[57] A. R. Palmer, D. Jiang, and D. McAlpine. Desynchronizing responses to correlated noise: a mechanism for binaural masking level differences at the inferior colliculus. *Journal of Neurophysiology*, 81(2):722–734, 1999.

[58] I. Siveke, C. Leibold, and B. Grothe. Spectral composition of concurrent noise affects neuronal sensitivity to interaural time differences of tones in the dorsal nucleus of the lateral lemniscus. *Journal of Neurophysiology*, 98(5):2705–2715, 2007.

[59] R. Batra, S. Kuwada, and D. C. Fitzpatrick. Sensitivity to interaural temporal disparities of low- and high-frequency neurons in the superior olivary complex. I. Heterogeneity of responses. *Journal of Neurophysiology*, 78(3):1222–1236, 1997.

[60] M. Pecka, A. Brand, O. Behrend, and B. Grothe. Interaural time difference processing in the mammalian medial superior olive: the role of glycinergic inhibition. *The Journal of Neuroscience*, 28(27):6914–6925, 2008.

[61] S. Kuwada, D. C. Fitzpatrick, R. Batra, and E.-M. Ostapoff. Sensitivity to interaural time differences in the dorsal nucleus of the lateral lemniscus of the unanesthetized rabbit: comparison with other structures. *Journal of Neurophysiology*, 95(3):1309–1322, 2006.

[62] L. A. Jeffress. A place theory of sound localization. *Journal of Comparative and Physiological Psychology*, 41(1):35–39, 1948.

[63] P. Berens. CircStat: a MATLAB toolbox for circular statistics. *Journal of Statistical Software*, 31(10):1–21, 2009.

[64] J. P. Agapiou and D. McAlpine. Low-frequency envelope sensitivity produces asymmetric binaural tuning curves. *Journal of Neurophysiology*, 100(4):2381–2396, 2008.

[65] V. N. Vapnik. *Statistical learning theory*. Wiley, New York, 1998.

[66] S. Sonnenburg, G. Rätsch, C. Schäfer, and B. Schölkopf. Large scale multiple kernel learning. *Journal of machine learning research*, 7(7):1531–1565, 2006.

[67] R. S. Heffner and H. E. Heffner. Sound localization and use of binaural cues by the gerbil (meriones unguiculatus). *Behavioral Neuroscience*, 102(3):422–428, 1988.

[68] N. A. Lesica, A. Lingner, and B. Grothe. Population coding of interaural time differences in gerbils and barn owls. *The Journal of Neuroscience*, 30(35):11696–11702, 2010.

[69] B. Kollmeier, G. Klump, V. Hohmann, U. Langemann, M. Mauermann, S. Uppenkamp, and J. Verhey. *Hearing from sensory processing to perception*. Springer, Berlin, 2007.

[70] D. McAlpine, D. Jiang, and A. R. Palmer. Interaural delay sensitivity and the classification of low best-frequency binaural responses in the inferior colliculus of the guinea pig. *Hearing Research*, 97(1-2):136–152, 1996.

[71] R. Batra and D. C. Fitzpatrick. Processing of interaural temporal disparities in the medial division of the ventral nucleus of the lateral lemniscus. *Journal of Neurophysiology*, 88(2):666–675, 2002.

[72] M. Bethge, D. Rotermund, and K. Pawelzik. Second order phase rransition in neural rate coding: Binary encoding is optimal for rapid signal transmission. *Physical Review Letters*, 90(8):8–11, 2003.

[73] D. A. Butts and M. S. Goldman. Tuning curves, neuronal variability, and sensory coding. *PLoS Biology*, 4(4):e92, 2006.

[74] K. K. Glendenning and R. B. Masterton. Comparative morphometry of mammalian central auditory systems: variation in nuclei and form of the ascending system. *Brain Behavior and Evolution*, 51(2):59–89, 1998.

[75] C. Köppl. Phase locking to high frequencies in the auditory nerve and cochlear nucleus magnocellularis of the barn owl, tyto alba. *The Journal of Neuroscience*, 17(9):3312–3321, 1997.

[76] A. W. Mills. Desynchronizing responses to correlated noise: A mechanism for binaural masking level differences at the inferior colliculus. *Journal of the Acoustical Society of America*, 30:237–46, 1958.

[77] P. Joris and T. C. T. Yin. A matter of time: internal delays in binaural processing. *Trends in Neurosciences*, 30(2):70–78, 2007.

[78] Y. Zhou, L. H. Carney, and H. S. Colburn. A model for interaural time difference sensitivity in the medial superior olive: interaction of excitatory and inhibitory synaptic inputs, channel dynamics, and cellular morphology. *The journal of Neuroscience*, 25(12):3046–3058, 2005.

[79] C. Leibold and J. L. van Hemmen. Spiking neurons learning phase delays: how mammals may develop auditory time-difference sensitivity. *Physical Review Letters*, 94(16):2–5, 2005.

[80] C. Leibold. Influence of inhibitory synaptic kinetics on the interaural time difference sensitivity in a linear model of binaural coincidence detection. *Journal of the Acoustical Society of America*, 127(2):931–942, 2010.

[81] P. E. Jercog, G. Svirskis, V. C. Kotak, D. H. Sanes, and J. Rinzel. Asymmetric excitatory synaptic dynamics underlie interaural time difference processing in the auditory system. *PLoS Biology*, 8(6):e1000406, 2010.

[82] R. Schmidt, K. Diba, C. Leibold, D. Schmitz, G. Buzsáki, and R. Kempter. Single-trial phase precession in the hippocampus. *The Journal of Neuroscience*, 29(42):13232–13241, 2009.

[83] M. Konishi. Coding of auditory space. *Annual Review of Neuroscience*, 26:31–55, 2003.

[84] A. Moiseff and M. Konishi. Neuronal and behavioral sensitivity to binaural time differences in the owl. *The Journal of Neuroscience*, 1(1):40–48, 1981.

[85] C. E. Shannon and W. Weaver. *The Mathematical Theory of Communication*. University of Illinois Press, Illinois, 1949.

[86] H. B. Barlow. *Possible principles underlying the transformations of sensory messages.* MIT Press, Boston, 1961.

[87] S. Laughlin. A simple coding procedure enhances a neuron's information capacity. *Zeitung für Naturforschung*, 36(9-10):910–912, 1981.

[88] H. B. Barlow, T. P. Kaushal, and G. J. Mitchison. Finding minimum entropy codes. *Neural Computation*, 1(3):412–423, 1989.

[89] E. Schneidman, M. J. Berry, R. Segev, and W. Bialek. Weak pairwise correlations imply strongly correlated network states in a neural population. *Nature*, 440(7087):1007–1012, 2006.

[90] D. H. Perkel, G. L. Gerstein, and G. P. Moore. Neuronal spike trains and stochastic point processes. II. Simultaneous spike trains. *Biophysical Journal*, 7(4):419–440, 1967.

[91] W. Bialek, F. Rieke, R. R. de Ruyter van Steveninck, and D. Warland. Reading a neural code. *Science*, 252(5014):1854–1857, 1991.

[92] D. H. Perkel, G. L. Gerstein, and G. P. Moore. Neuronal spike trains and stochastic point processes. I. The single spike train. *Biophysical Journal*, 7(4):391–418, 1967.

[93] E. Domany, J. L. van Hemmen, and K. Schulten. Physics of Neural Networks. Springer, New York, 1994.

[94] W. Gerstner. *Pulsed neural networks*. MIT Press, Boston, 1998.

[95] J. W. Pillow, J. Shlens, L. Paninski, A. Sher, A. M. Litke, E. J. Chichilnisky, and E. P. Simoncelli. Spatio-temporal correlations and visual signalling in a complete neuronal population. *Nature*, 454(8):995–999, 2008.

[96] R. Waser. *Nanoelectronics and information technology*. Wiley, New York, 2003.

[97] V. A. Makarov, F. Panetsos, and O. De Feo. A method for determining neural connectivity and inferring the underlying network dynamics using extracellular spike recordings. *Journal of Neuroscience Methods*, 144(2):265–279, 2005.

[98] D. Yu, M. Righero, and L. Kocarev. Estimating topology of networks. *Physical Review Letters*, 97(18):188701, 2006.

[99] D. Yu and U. Parlitz. Driving a network to steady states reveals its cooperative architecture. *Europhysics Letters*, 81(4):48007, 2008.

[100] M. Timme. Revealing network connectivity from dynamics. *Physical Review Letters*, 98(22):10, 2006.

[101] K. J. Friston. Functional and effective connectivity in neuroimaging: a synthesis. *Human Brain Mapping*, 2(1-2):56–78, 1994.

[102] D. Goodman and R. Brette. Brian: a simulator for spiking neural networks in Python. *Frontiers in neuroinformatics*, 2(11):10, 2008.

[103] P. Dayan and L. F. Abbott. *Theoretical neuroscience*. MIT Press, Boston, 2001.

[104] E. Ganmor, R. Segev, and E. Schneidman. The architecture of functional interaction networks in the retina. *Journal of Neuroscience*, 31(8):3044–3054, 2011.

[105] J. T. Vogelstein, B. O. Watson, A. M. Packer, R. Yuste, B. Jedynak, and L. Paninski. Spike inference from calcium imaging using sequential monte carlo methods. *Biophysical Journal*, 97(2):636–655, 2009.

[106] O. Stetter, D. Battaglia, J. Soriano, and T. Geisel. Model-Free Reconstruction of the Connectivity of Neuronal Networks from Calcium Imaging Signals (in preparation).